Instabilities of an anisotropically expanding non-Abelian plasma: 1D + 3V discretized hard-loop simulations

Anton Rebhan,[1] Michael Strickland,[2,3] and Maximilian Attems[1]

[1]*Institut für Theoretische Physik, Technische Universität Wien, Wiedner Hauptstraße 8-10, A-1040 Vienna, Austria*
[2]*Frankfurt Institute for Advanced Studies, Johann Wolfgang Goethe University, Max-von-Laue-Straße 1, D-60438 Frankfurt am Main, Germany*
[3]*Kavli Institute for Theoretical Physics, University of California Santa Barbara, Santa Barbara, California 93106, USA*

(Received 30 April 2008; published 21 August 2008)

Non-Abelian plasma instabilities play a crucial role in the nonequilibrium dynamics of a weakly coupled quark-gluon plasma, and they importantly modify the standard perturbative bottom-up thermalization scenario in heavy-ion collisions. Using the auxiliary-field formulation of the hard-loop effective theory, we study numerically the real-time evolution of instabilities in an anisotropic collisionless Yang-Mills plasma undergoing longitudinal free-streaming expansion. In this first real-time lattice simulation we consider the most unstable modes, long-wavelength coherent color fields that are constant in transverse directions and which therefore are effectively 1 + 1 dimensional in space-time, except for the auxiliary fields which also depend on discretized momentum rapidity and transverse velocity components. We reproduce the semianalytical results obtained previously for the Abelian regime, and we determine the nonlinear effects which occur when the instabilities have grown such that non-Abelian interactions become important.

DOI: 10.1103/PhysRevD.78.045023 PACS numbers: 12.38.Mh, 11.10.Wx, 11.15.Ha

I. INTRODUCTION

The experimental results obtained at the Relativistic Heavy Ion Collider (RHIC) [1] and their good agreement with hydrodynamical simulations with extremely early thermalization and a low shear viscosity [2–4] close to a conjectured lower quantum theoretical bound [5] are now widely interpreted as evidence that the hypothetical quark-gluon matter produced at RHIC is strongly interacting and very far from a perturbatively accessible regime. Indeed, perturbative approaches like that of the original bottom-up thermalization scenario [6–8] do not seem to be able to come close to explaining the fast apparent thermalization. However, as pointed out first by Ref. [9], the original bottom-up scenario is qualitatively changed by the inevitable presence of non-Abelian (chromo-Weibel) plasma instabilities [10–12] in a weakly coupled quark-gluon plasma with momentum-space anisotropy, although how the bottom-up scenario will have to be modified is still an open theoretical question, even at asymptotically weak coupling and in the first stage of the bottom-up scenario [13–17]. Non-Abelian plasma instabilities have moreover been argued to importantly modify weak-coupling results on the shear viscosity to anomalously low values [18]. Even if the quark-gluon matter produced at the RHIC may be too close to the deconfinement phase transition for any extrapolations of weak-coupling results, it is clearly necessary to better understand the latter and how they differ from other approaches. Finally, it may be the case that the higher energies to be reached at upcoming heavy-ion collider experiments at the CERN Large Hadron Collider (LHC) open the window to the specific collective phenomena of a weakly coupled quark-gluon plasma, such as non-Abelian plasma instabilities.

In this paper we shall discuss only the theoretically clean situation at asymptotically weak coupling and the dynamical evolution of non-Abelian plasma instabilities in a collisionless plasma with long-wavelength color fields. Any amount of momentum anisotropy in the distribution of the (high-momentum) plasma particles leads to chromomagnetic instabilities, which in the weak-field situation are straightforward generalizations of the Abelian Weibel instabilities [19] and whose dispersion laws have been worked out for specific cases of a stationary anisotropic plasma in Refs. [20–23]. In an Abelian plasma, the Weibel instabilities grow exponentially until they are large enough to modify the distribution of the hard particles and give rise to their fast isotropization. In a weakly coupled non-Abelian plasma, the situation is more complicated because the long-wavelength color fields have nonlinear self-interactions before they reach the size where fast isotropization occurs. The first numerical simulations [24] of non-Abelian plasma instabilities using the systematic framework of the hard-loop effective theory [25–28] have concentrated on the most unstable modes which are constant in the directions transverse to the direction of momentum anisotropy. It was found that such configurations experience a certain amount of Abelianization over domains of finite size when they enter the nonlinear regime, which allows them to continue an exponential growth out of the hard-loop regime, confirming essentially the conjecture of Ref. [29] formed from numerical studies of a toy model

which showed virtually complete Abelianization. In spacetime, the corresponding evolution equations are $1+1$ dimensional, and in the hard-loop effective theory are coupled to auxiliary fields that depend on the three-dimensional velocity of the hard particles, so that in conventional plasma physics these simulations would be termed 1D + 3V. Fully $3+1$-dimensional simulations (3D + 3V) later showed, however, that more generic field configurations in a plasma with fixed (moderate) momentum-space anisotropy do not continue to grow exponentially in the strong-field regime, but enter a linear-growth phase [30,31] by the formation of a cascade which pumps the growing energy in the infrared modes into higher-momentum modes [15,32]. The recent simulations of Ref. [33], however, found a continued exponential growth of initially small perturbations in the case of very strong momentum anisotropy. A very strong anisotropy (if not the requirement of initially small fluctuations [17]) is of particular interest for heavy-ion collision where in a weak-coupling situation the longitudinal expansion makes longitudinal momenta of quarks and gluons much smaller than their transverse momenta.

Recently, in Ref. [34] the hard-loop effective theory for stationary anisotropic plasmas was extended to the case of a boost-invariant, longitudinally expanding distribution of plasma particles, the hard-expanding-loop (HEL) effective theory. The essentially Abelian weak-field regime was worked out semianalytically with the result that the counterplay of increasing anisotropy and decreasing plasma density lets Weibel instabilities grow exponentially in the square root of proper time, with more and more modes becoming unstable as time goes on, but each one experiencing a certain delay before growth kicks in. A similar behavior was previously found in numerical studies of initially small rapidity fluctuations in the so-called color-glass-condensate framework [35,36]. By matching the mass scales involved with the parameters of the saturation scenario [37], the conclusion was drawn that LHC energies will be needed to allow for conditions where strong quark-gluon-plasma instabilities can develop from small initial rapidity fluctuations, leaving open, however, the issue of strong initial gauge fields.

In the present paper we begin the study of the evolution of genuinely non-Abelian plasma instabilities in a longitudinally expanding plasma by a lattice discretization of the HEL theory and 1D + 3V simulations. The latter have been found to give an upper limit of the full $3+1$-dimensional evolution of more generic field configurations. The results of [33] for strong anisotropy suggest that this upper limit may well be reached by $3+1$-dimensional plasma instabilities that start out as small rapidity fluctuations (though not for those that are initially nonperturbatively large). The 3D + 3V (as well as 2D + 3V [38]) real-time lattice simulations of the HEL theory, which will be needed to address also initially strong rapidity fluctuations, will be the subject of follow-up work.

II. HARD-LOOP EFFECTIVE FIELD EQUATIONS FOR AN ANISOTROPICALLY EXPANDING NON-ABELIAN PLASMA

For an ultrarelativistic plasma, a sufficiently small (gauge) coupling g introduces a hierarchy of scales, separating the hard momenta $|\mathbf{p}| = p^0$ of plasma constituents from the "soft" scale $\sim g\sqrt{f}|\mathbf{p}|$, where f is the typical hard particle occupation number (which may be different from order one in strongly nonequilibrium situations). The soft scale is associated with various screening phenomena and the various branches of plasmon propagation. Ultrasoft scales $\sim g^2 f|\mathbf{p}|$ are responsible for the damping of quasiparticles and, in or close to thermal equilibrium, for the nonperturbative screening of chromomagnetostatic fields.

In an anisotropic plasma, the perturbatively accessible soft scale is also responsible for plasma instabilities, which constitute the dominant nonequilibrium effects at weak coupling: the associated rates are parametrically larger than any of the scattering processes, even though the latter are enhanced in a non-Abelian plasma.[1] As long as the amplitude of the gauge fields $A \ll \sqrt{f}|\mathbf{p}|$, the evolution of the plasma instabilities is essentially Abelian and can be studied by a perturbative linear response analysis. For a stationary anisotropic plasma, the evolution is simply exponential in time. When the amplitude becomes nonperturbatively large, $A \gtrsim \sqrt{f}|\mathbf{p}|$, non-Abelian self-interactions of the gauge fields become important to leading order and require numerical evaluation, which as long as $A \ll |\mathbf{p}|/g$ can be carried out consistently within the hard-loop effective field theory framework.[2] In the latter, the hard particles are integrated out to produce a nonlocal and highly nonlinear effective action which can be written in terms of a compact integral representation [43–45]. This was initially obtained for the case of thermal equilibrium and has a straightforward generalization to the case of stationary momentum-space anisotropy [26,28]. It is of particular importance to numerical lattice studies that the corresponding effective field equations can be made local at the expense of introducing a continuous set of auxiliary fields [46] which arise naturally when solving gauge-covariant Boltzmann-Vlasov equations [25,47–49]. In the hard-loop approximation, these auxiliary fields depend on the velocity vector of the hard particles whose hard momentum scale is integrated out.

In Ref. [34] this approach was extended to the case of a nonstationary plasma with a free-streaming expanding dis-

[1]As we shall see below, for strongly anisotropic plasmas the relevant soft-scale parameters also depend importantly on the anisotropy parameter(s) hidden in f.

[2]For numerical simulations which take into account the back-reaction of the soft fields on the hard particles that come into play when $A \sim |\mathbf{p}|/g$ using a Boltzmann-Vlasov treatment, see Refs. [39–41]; for numerical simulations which include back-reaction using a statistical classical field theory treatment, see Refs. [35,36,42].

tribution of hard particles, which we first review, filling in some details left out in Ref. [34], before proceeding with numerical real-time lattice calculations. The latter allows us to follow the time evolution of plasma instabilities with initially small fields into the regime where non-Abelian self-interactions become important. The key difference from previous hard-loop simulations of non-Abelian plasma instabilities [24,30,31,33] is in the time dependence of the (soft-scale) parameters which determine the growth rate of a given unstable mode and also which modes are unstable.

A. Gauge-covariant Boltzmann-Vlasov equations in a nonstationary plasma

Assuming a color neutral background distribution function $f_0(\mathbf{p}, \mathbf{x}, t)$ which satisfies

$$v \cdot \partial f_0(\mathbf{p}, \mathbf{x}, t) = 0, \qquad v^\mu = p^\mu/p^0, \tag{1}$$

the gauge-covariant Boltzmann-Vlasov equations for colored perturbations δf_a of an approximately collisionless plasma have the form

$$v \cdot D\delta f_a(\mathbf{p}, \mathbf{x}, t) = g v_\mu F_a^{\mu\nu} \partial_\nu^{(p)} f_0(\mathbf{p}, \mathbf{x}, t), \tag{2}$$

and have to be solved self-consistently with the non-Abelian Maxwell equations

$$D_\mu F_a^{\mu\nu} = j_a^\nu = g t_R \int \frac{d^3p}{(2\pi)^3} \frac{p^\mu}{2p^0} \delta f_a(\mathbf{p}, \mathbf{x}, t). \tag{3}$$

Here t_R is a suitably normalized group factor, while the total number of degrees of freedom of the hard particles is taken care of by the normalization of the distribution function f_0.

In a stationary (but possibly anisotropic) plasma, f_0 only depends on momenta, and (1) is satisfied trivially. Here we shall consider the generalization to a plasma which expands longitudinally, which should be a good approximation for the initial stage of a parton gas produced in a heavy-ion collision as long as the transverse dimension of the system is sufficiently large. Assuming, furthermore, boost invariance in rapidity [50] and isotropy in the transverse directions, the unperturbed distribution function f_0, being a Lorentz scalar, has the form [51,52]

$$f_0(\mathbf{p}, x) = f_0(p_\perp, p^z, z, t) = f_0(p_\perp, p'^z, \tau) \tag{4}$$

where the transformed longitudinal momentum is

$$\begin{aligned} p'^z &= \gamma(p^z - \beta p^0), \qquad \beta = z/t, \\ \gamma &= t/\tau, \qquad \tau = \sqrt{t^2 - z^2}, \end{aligned} \tag{5}$$

with $p^0 = \sqrt{p_\perp^2 + (p^z)^2}$ for ultrarelativistic (massless) particles.

B. Comoving coordinates

It is convenient to switch to comoving coordinates

$$\begin{aligned} t &= \tau\cosh\eta, \qquad \beta = \tanh\eta, \\ z &= \tau\sinh\eta, \qquad \gamma = \cosh\eta, \end{aligned} \tag{6}$$

i.e. a coordinate system with metric $ds^2 = d\tau^2 - d\mathbf{x}_\perp^2 - \tau^2 d\eta^2$. We introduce the notation $\tilde{x}^\alpha = (x^\tau, x^i, x^\eta) = (\tau, x^1, x^2, \eta)$ with indices from the beginning of the Greek alphabet for these new coordinates. Note that in the latter the indices $i, j, \ldots$ are restricted to the two transverse spatial coordinates.

In what follows we shall not deal with space-time covariant derivatives and Christoffel symbols, but write everything in terms of explicit derivatives. In particular, the gauge-covariant derivative always means[3] $\tilde{D}_\alpha = \tilde{\partial}_\alpha - ig[\tilde{A}_\alpha, \cdot]$. Being a two-form (where indices are naturally down), the field strength retains its usual form: $\tilde{F}_{\alpha\beta} = \tilde{\partial}_\alpha \tilde{A}_\beta - \tilde{\partial}_\beta \tilde{A}_\alpha - ig[\tilde{A}_\alpha, \tilde{A}_\beta]$. The (non-Abelian) Maxwell equations do involve additional terms, but they can be written compactly as

$$\frac{1}{\tau}\tilde{D}_\alpha(\tau\tilde{F}^{\alpha\beta}) \equiv \frac{1}{\tau}\tilde{D}_\alpha[\tau g^{\alpha\gamma}(\tau) g^{\beta\delta}(\tau)\tilde{F}_{\gamma\delta}] = \tilde{j}^\beta. \tag{7}$$

In addition to space-time rapidity η, we also introduce momentum-space rapidity y for the massless particles according to

$$p^\mu = p_\perp(\cosh y, \cos\phi, \sin\phi, \sinh y). \tag{8}$$

In comoving coordinates (with tildes), we then have

$$\begin{aligned} \tilde{p}^\tau &= \sqrt{p_\perp^2 + \tau^2(\tilde{p}^\eta)^2} = \cosh\eta p^0 - \sinh\eta p^z \\ &= p_\perp\cosh(y - \eta), \end{aligned} \tag{9}$$

$$\begin{aligned} \tilde{p}^\eta &= -\tilde{p}_\eta/\tau^2 = (\cosh\eta p^z - \sinh\eta p^0)/\tau \\ &= p'^z/\tau = p_\perp\sinh(y - \eta)/\tau. \end{aligned} \tag{10}$$

Instead of the lightlike vector $v^\mu = p^\mu/p^0$ containing a unit 3-vector that was used in Eqs. (1) and (2), we shall define the new quantity

$$\tilde{V}^\alpha = \frac{\tilde{p}^\alpha}{p_\perp} = \left(\cosh(y - \eta), \cos\phi, \sin\phi, \frac{1}{\tau}\sinh(y - \eta)\right), \tag{11}$$

which is normalized so that it has a unit 2-vector in the transverse plane.

[3]Recall that $A^\mu = (\phi, \vec{A})$ with 4-index up. Thus $\tilde{A}_\alpha = (A_\tau, -A^x, -A^y, A_\eta)$.

C. Longitudinally expanding, free-streaming background solution

Equation (1), involving space-time derivatives at fixed $\mathbf{p}_\perp$ and p^z, can be rewritten as

$$(\tilde{p}\cdot\tilde{\partial})f_0|_{y,\mathbf{p}_\perp}=0. \tag{12}$$

Because

$$\begin{aligned}\tilde{p}^\tau\partial_\tau\tilde{p}_\eta(\tilde{x})|_{y,\mathbf{p}_\perp}&=-p_\perp^2\sinh(y-\eta)\cosh(y-\eta)\\&=-\tilde{p}^\eta\partial_\eta\tilde{p}_\eta(\tilde{x})|_{y,\mathbf{p}_\perp}\end{aligned} \tag{13}$$

this can be solved by $f_0(\mathbf{p},\mathbf{x},t)=f_0(\mathbf{p}_\perp,\tilde{p}_\eta(x))=f_0(\mathbf{p}_\perp,-p'^z(x)\tau(x))$.

In the following we shall use[4]

$$f_0(\mathbf{p},x)=f_{\rm iso}\left(\sqrt{p_\perp^2+\left(\frac{p'^z\tau}{\tau_{\rm iso}}\right)^2}\right)=f_{\rm iso}(\sqrt{p_\perp^2+\tilde{p}_\eta^2/\tau_{\rm iso}^2}) \tag{14}$$

which corresponds to local isotropy on the hypersurface $\tau=\tau_{\rm iso}$, and increasingly oblate momentum-space anisotropy at $\tau>\tau_{\rm iso}$ (but prolate anisotropy for $\tau<\tau_{\rm iso}$). Since a plasma description does not make sense at arbitrarily small times and time evolution will have to start at a nonzero proper time τ_0, the time $\tau_{\rm iso}$ may be entirely fictitious in the sense of pertaining to the preplasma (glasma [36,53]) phase. This will in fact be the case in the numerical simulations below, where we shall start already with oblate anisotropy by choosing $\tau_{\rm iso}<\tau_0$.

In a comoving frame, the energy density and pressure components of the hard particle background can be determined by evaluating $T^{\alpha\beta}_{\rm part.}=(2\pi)^{-3}\int d^2p_\perp dy\tilde{p}^\alpha\tilde{p}^\beta f_0$, which yields

$$\mathcal{E}_{\rm part.}(\tau)=T^{\tau\tau}_{\rm part.}=\frac{1}{2}\left[\frac{1}{\bar{\tau}^2}+\frac{\arcsin\sqrt{1-\bar{\tau}^{-2}}}{\sqrt{\bar{\tau}^2-1}}\right]\mathcal{E}_{\rm iso}, \tag{15}$$

$$\begin{aligned}P_T^{\rm part.}(\tau)&=\frac{1}{2}T^{ii}_{\rm part.}\\&=\frac{1}{4(\bar{\tau}^2-1)}\left[1+\frac{\bar{\tau}^2-2}{\sqrt{\bar{\tau}^2-1}}\arcsin\sqrt{1-\bar{\tau}^{-2}}\right]\mathcal{E}_{\rm iso},\end{aligned} \tag{16}$$

$$\begin{aligned}P_L^{\rm part.}(\tau)&=-T^\eta_{{\rm part.}\,\eta}\\&=\frac{1}{2(\bar{\tau}^2-1)}\left[-\frac{1}{\bar{\tau}^2}+\frac{\arcsin\sqrt{1-\bar{\tau}^{-2}}}{\sqrt{\bar{\tau}^2-1}}\right]\mathcal{E}_{\rm iso},\end{aligned} \tag{17}$$

where $\mathcal{E}_{\rm iso}=\mathcal{E}_{\rm part.}(\tau_{\rm iso})$, $\bar{\tau}\equiv\tau/\tau_{\rm iso}$, assuming $\bar{\tau}\geq 1$. For $\bar{\tau}\gg 1$ we have

$$P_T^{\rm part.}\to\frac{\pi}{8}\mathcal{E}_{\rm iso}\bar{\tau}^{-1},\qquad P_L^{\rm part.}\to\frac{\pi}{4}\mathcal{E}_{\rm iso}\bar{\tau}^{-3}. \tag{18}$$

The energy density follows from $\mathcal{E}_{\rm part.}\equiv 2P_T^{\rm part.}+P_L^{\rm part.}$.

The particle distribution function (14) has the same form as the one used in Refs. [20,21,24,31], but the anisotropy parameter ξ therein[5] is now space-time dependent according to

$$\xi(\tau)=(\tau/\tau_{\rm iso})^2-1, \tag{19}$$

and the normalization factor $N(\xi)$ of Refs. [21,24,31] is unity.

The behavior $\xi\sim\tau^2$ at large τ is a consequence of having a free-streaming background distribution. In a more realistic collisional plasma, ξ will have to grow slower than this. In the first stage of the original bottom-up scenario [13], ignoring plasma instabilities, one would have had $\xi\sim\tau^{2/3}$. In Ref. [14] it was argued that plasma instabilities reduce the exponent to $\xi\sim\tau^{1/2}$, whereas Ref. [17] recently presented arguments in favor of $\xi\sim\tau^{1/4}$. All these scenarios have $\xi\gg 1$, so below we shall concentrate on the case $\tau_{\rm iso}<\tau_0$ and thus high anisotropy for all $\tau>\tau_0$, but in the idealized case of a collisionless free-streaming expansion.

D. HEL effective field equations

Transforming the gauge-covariant Vlasov equation to comoving coordinates, one can write

$$\tilde{V}\cdot\tilde{D}\delta f^a|_{p^\mu}=g\tilde{V}^\alpha\tilde{F}^a_{\alpha\beta}\tilde{\partial}^\beta_{(p)}f_0(\mathbf{p}_\perp,\tilde{p}_\eta), \tag{20}$$

where the derivative on the left-hand side has to be taken at fixed p^μ as opposed to fixed $\tilde{p}^\alpha$. On the right-hand side the derivative with respect to momenta is at fixed x, but the transformation from x to $\tilde{x}$ does not depend on momenta anyway. However, in the following it will be important to write the right-hand side in terms of $\tilde{\partial}^\beta_{(p)}f_0(\mathbf{p}_\perp,\tilde{p}_\eta)$ with index up so that this factor depends only on $\mathbf{p}_\perp$ and $\tilde{p}_\eta$ and not additionally on τ. This means, in particular, that $p\cdot\partial(\tilde{\partial}^\beta_{(p)}f_0)|_p=\tilde{p}\cdot\tilde{\partial}(\tilde{\partial}^\beta_{(p)}f_0)|_p=0$.

Equation (20) can then be solved in terms of an auxiliary field $\tilde{W}_\beta(\tilde{x};\phi,y)$ which satisfies

$$\tilde{V}\cdot\tilde{D}\tilde{W}_\beta|_{\phi,y}=\tilde{V}^\alpha\tilde{F}_{\beta\alpha} \tag{21}$$

and

$$\delta f(x;p)=-g\tilde{W}_\beta(\tilde{x};\phi,y)\tilde{\partial}^\beta_{(p)}f_0(p_\perp,\tilde{p}_\eta). \tag{22}$$

The field $\tilde{W}_\beta(\tilde{x};\phi,y)$ is indeed analogous to the auxiliary field $W_\nu(x;\mathbf{v})$ of the (static-background) hard-loop formalism [28] because, for a given space-time point, it

[4]Notice that it would be straightforward to relax the assumption of momentum-space isotropy in the transverse directions.

[5]The anisotropy parameter θ used in Ref. [17] is related to ξ by $\xi\sim\theta^{-2}$.

only depends on the 3-velocity of the hard particles, $\mathbf{v} = (\cos\phi, \sin\phi, \sinh y)/\cosh y$, and not on their energy p^0. Notice that only with index down is its equation of motion (21) formally the same as in the static situation.

Expressed in terms of the auxiliary field $\tilde{W}$, the induced current in comoving coordinates reads

$$\begin{aligned}\tilde{j}^{\alpha}[A] &= -\frac{g^2 t_R}{2}\int\frac{d^3p}{(2\pi)^3}\frac{1}{p^0}\tilde{p}^{\alpha}\frac{\partial f_0(p_\perp,\tilde{p}_\eta)}{\partial\tilde{p}_\beta}\tilde{W}_\beta(\tilde{x};\phi,y)\\ &= +g^2 t_R\int\frac{d^2p_\perp dp_\eta}{(2\pi)^3}\frac{1}{2\tau p^\tau}\tilde{p}^{\alpha}\frac{\partial f_0(p_\perp,\tilde{p}_\eta)}{\partial\tilde{p}_\beta}\tilde{W}_\beta\\ &= -g^2 t_R\int_0^\infty\frac{p_\perp dp_\perp}{8\pi^2}\int_0^{2\pi}\frac{d\phi}{2\pi}\int_{-\infty}^{\infty}dy\tilde{p}^{\alpha}\frac{\partial f_0}{\partial\tilde{p}_\beta}\tilde{W}_\beta\end{aligned} \tag{23}$$

where for each (ϕ, y) (i.e., fixed $\mathbf{v}$) the scale $p_\perp$ (related to energy by $p^0 = p_\perp\cosh y$) can be integrated out.

With a distribution function that is even in $\mathbf{p}_\perp$ and $\tilde{p}_\eta$ as in (14), covariant current conservation can be verified without having to integrate partially with respect to p. (This proves to be helpful for the lattice discretization below, where all integrals will be replaced by discrete sums.) The current j^μ in ordinary coordinates is given by Eq. (23) by dropping the tilde on $\tilde{j}^\alpha$ and $\tilde{p}^\alpha$ only. Starting from the first line of (23), we can then use $D\cdot p = p\cdot D = \tilde{p}\cdot\tilde{D}$ and $(p\cdot\partial)\partial f_0/\partial\tilde{p}_\beta|_p = 0$, and finally (21) (with $\tilde{V}$ replaced by $\tilde{p}^\alpha$). Changing the integration variables to $\tilde{p}$ like in the second line of (23), we obtain

$$\begin{aligned}D\cdot j = g^2 t_R\int\frac{d^2p_\perp dp_\eta}{(2\pi)^3}&\frac{1}{2\tau\sqrt{p_\perp^2+p_\eta^2/\tau^2}}\\ &\times\left[\frac{\partial f_0}{\partial p^i}\tilde{F^i}_\gamma\tilde{p}^\gamma+\frac{\partial f_0}{\partial p_\eta}\tilde{F}_{\eta\gamma}\tilde{p}^\gamma\right].\end{aligned}$$

This vanishes already by symmetry when $\partial f_0/\partial p^i$ and $\partial f_0/\partial p_\eta$ are odd functions in p^i and p_η, respectively.

Specializing to the background distribution function (14), we have

$$\begin{aligned}\tilde{\partial}^{\beta}_{(p)}f_0 &= f_0'\tilde{\partial}^{\beta}_{(p)}\sqrt{p_\perp^2+\tilde{p}_\eta^2/\tau_{\rm iso}^2}\\ &= \frac{(0,-\cos\phi,-\sin\phi,-\frac{\tau}{\tau_{\rm iso}^2}\sinh(y-\eta))}{\sqrt{1+\frac{\tau^2}{\tau_{\rm iso}^2}\sinh^2(y-\eta)}},\end{aligned} \tag{24}$$

and we get

$$\begin{aligned}\tilde{j}^{\alpha} = -m_D^2\frac{1}{2}\int_0^{2\pi}\frac{d\phi}{2\pi}\int_{-\infty}^{\infty}dy\tilde{V}^{\alpha}\\ \times\left(1+\frac{\tau^2}{\tau_{\rm iso}^2}\sinh^2(y-\eta)\right)^{-2}\mathcal{W}(\tilde{x};\phi,y),\end{aligned} \tag{25}$$

where

$$\mathcal{W} = \tilde{V}^i W_i - \frac{1}{\tau_{\rm iso}^2}\tilde{V}_\eta\tilde{W}_\eta,\qquad \tilde{V}^i = (\cos\phi,\sin\phi),$$
$$\tilde{V}_\eta = -\tau\sinh(y-\eta), \tag{26}$$

and

$$m_D^2 = -g^2 t_R\int_0^\infty\frac{dpp^2}{(2\pi)^2}f'_{\rm iso}(p). \tag{27}$$

The mass parameter m_D equals the Debye mass at the (possibly fictitious because of preplasma) time $\tau_{\rm iso}$.

Because $\tilde{V}\cdot\tilde{D}$ commutes with the coefficients of $\tilde{W}_i$ and $\tilde{W}_\eta$ appearing in the definition of $\mathcal{W}$ [in particular, $[\tilde{V}\cdot\tilde{D},\tilde{V}_\eta]=0$, cf. (13)], we do not need to evolve the components $\tilde{W}_\beta$ separately, but only the combination $\mathcal{W}$, which is governed by

$$\begin{aligned}\tilde{V}\cdot\tilde{D}\mathcal{W} = &\left(\tilde{V}^i\tilde{F}_{i\tau}+\frac{\tau^2}{\tau_{\rm iso}^2}\tilde{V}^\eta\tilde{F}_{\eta\tau}\right)\tilde{V}^\tau\\ &+\tilde{V}^i\tilde{V}^\eta\tilde{F}_{i\eta}\left(1-\frac{\tau^2}{\tau_{\rm iso}^2}\right).\end{aligned} \tag{28}$$

For $\tau = \tau_{\rm iso}$ only $F_{\alpha\tau}$ (the electric field components in the comoving frame[6]) appear on the right-hand side, whereas for $\tau = \tau_{\rm iso}$ magnetic fields come into play, opening the door for magnetic instabilities.

This single equation for $\mathcal{W}$ together with the Yang-Mills equations and the algebraic relation between j and $\mathcal{W}$ close our equations of motion. To solve them, we adopt the comoving temporal gauge $A^\tau = 0$ and introduce canonical conjugate field momenta for the remaining gauge fields according to

$$\Pi^i = \tau\partial_\tau A_i = -\tau\partial_\tau A^i = -\Pi_i \tag{29}$$

and

$$\Pi^\eta = \frac{1}{\tau}\partial_\tau A_\eta. \tag{30}$$

Notice that transverse (comoving) electric field components differ from Π^i by a factor of τ:

$$E^i = \tau^{-1}\Pi^i. \tag{31}$$

In contrast to most of the literature on the color-glass-condensate framework, we shall reserve the symbol E for the electric field and denote the canonical conjugate field momenta by Π.

In terms of fields and conjugate momenta, the Yang-Mills equations take the form

$$\tau\partial_\tau\Pi^\eta = j_\eta - D_i F^i{}_\eta, \tag{32}$$

$$\tau^{-1}\partial_\tau\Pi_i = j^i - D_j F^{ji} - D_\eta F^{\eta i}. \tag{33}$$

[6]From here on we shall drop the tilde on the quantities in the comoving frame, which will be used exclusively in what follows.

E. 1D + 3V equations

A linear response analysis (appropriate for small gauge field amplitudes) shows that the most unstable modes of an anisotropic plasma are those whose wave vectors are oriented along the direction of anisotropy.

We therefore begin by considering only initial conditions and thus solutions which are constant in the transverse directions (i.e., neglecting transverse dynamics), $\partial_i A^\alpha \equiv 0$. Hence, $D^i = -ig[A^i, \cdot]$ and the Yang-Mills equations reduce to that of a 1 + 1-dimensional theory with A^i acting as adjoint scalars.

We then have

$$\frac{1}{\tau}\partial_\tau \Pi_i = j^i + g^2 i[A^j, i[A^j, A^i]] + \frac{1}{\tau^2} D_\eta^2 A^i, \tag{34}$$

$$\tau \partial_\tau \Pi^\eta = j_\eta + ig[A^i, D_\eta A^i], \tag{35}$$

as dynamical Yang-Mills equations, and

$$\tau j^\tau = D_\eta \Pi^\eta - ig[A^i, \Pi_i] \tag{36}$$

as the Gauss law constraint.

The current j^α is a linear functional of $\mathcal{W}$, given by Eq. (25) as before, but the equation of motion for $\mathcal{W}$, Eq. (28), reduces to

$$\begin{aligned}\partial_\tau \mathcal{W}(\tau, \eta; \phi, y) = &\frac{\tanh(y-\eta)}{\tau} D_\eta \left(\left(1 - \frac{\tau^2}{\tau_{\rm iso}^2}\right) v^i A^i - \mathcal{W}\right) \\ &- \frac{ig}{\cosh(y-\eta)}[v^i A^i, \mathcal{W}] \\ &+ \frac{1}{\tau} v^i \Pi_i - \frac{\tau^2 \sinh(y-\eta)}{\tau_{\rm iso}^2} \Pi^\eta. \end{aligned} \tag{37}$$

All fields here depend on the two remaining space-time variables τ, η, and the auxiliary adjoint-scalar field $\mathcal{W}$ additionally depends on the momentum-space variables ϕ, y which parametrize the 3-velocity in the colored fluctuations δf^a; cf. Eq. (22).

In the present paper we shall restrict our attention to this dimensionally reduced situation, which in conventional plasma literature would be referred to as 1D + 3V. The study of 2D + 3V and 3D + 3V is postponed to future publications.

III. LATTICE DISCRETIZATION AND NUMERICAL RESULTS

A. Methods

For a numerical evaluation of Eqs. (34)–(37) together with Eq. (25), we discretize proper time starting with finite $\tau_0 > 0$ and time step ϵ. The space-time rapidity coordinate η is made periodic and discrete with N_η points and (dimensionless) spacing a covering a rapidity interval $(-N_\eta a/2, N_\eta a/2)$. The (matrix-valued) fields A^x, A^y, and $\mathcal{W}_{\phi,y}$ are defined on the sites of the one-dimensional rapidity lattice, while the conjugate momenta Π_x, Π_y, and Π^η are defined on the temporal links. The gauge field A_η is replaced by the spatial link variable $U = \exp igaA_\eta$.

The integration over the momentum-space variables ϕ and y in Eq. (25) has to be discretized such that covariant current conservation is preserved manifestly. When expressed in terms of ϕ and y integrals, the integrand in (24) is either odd in $y - \eta$ or multiplied by $\sin\phi$ or $\cos\phi$. In order that discretization of y and ϕ respect manifest covariant current conservation, we thus need to respect reflection invariance in ϕ and $y - \eta$. The angular variable is made discrete with uniform spacing $2\pi/N_\phi$, but for $\bar{y} \equiv y - \eta$ we shall consider two possibilities. In method A we shall discretize the interval $-\Lambda_y \le \bar{y} \le \Lambda_y$ uniformly with spacing $2\Lambda_y/(N_y + 1)$, and in method B we make the substitution $\bar{y} = \operatorname{atanh} x$ and discretize the range $-1 + \Delta x \le x \le 1 - \Delta x$ with uniform spacing $\Delta x = 1/N_x$. Because of the η dependence of the shifted variable $\bar{y}$, the lattice equation of motion for the auxiliary fields $\mathcal{W}_{\phi,\bar{y}}$ that live on the $\bar{y}$ boundary has to be completed by boundary conditions for $\mathcal{W}$ in the $\bar{y}$ variable. For the $\mathcal{W}$ fields we do not impose periodicity, but instead take the Neumann condition $\partial \mathcal{W}/\partial \bar{y} = 0$ at the $\bar{y}$ boundary.

In Fig. 1 we show the evolution of the conjugate momentum $\Pi_x \propto \cos(\nu\eta)$ in the case that the gauge group is taken to be Abelian U(1). The system is initialized with a single Abelian U(1) mode with only Π_x initialized with rapidity wave number $\nu = 16\pi/5 = 10.053\ldots$ in order to facilitate comparisons with semianalytic results obtained

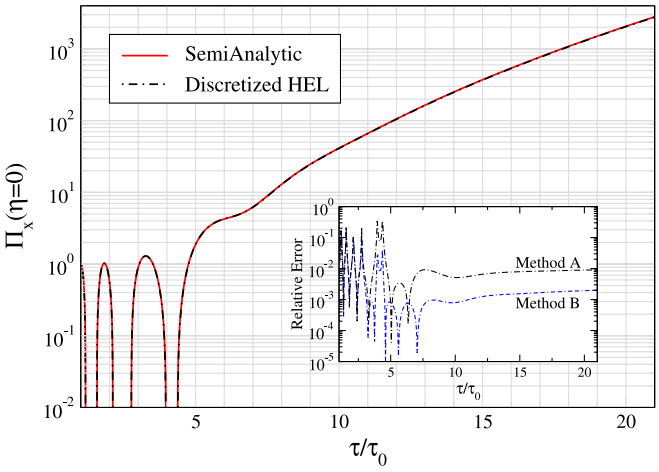

FIG. 1 (color online). Proper-time evolution of the canonical field momentum $\Pi_x(\eta = 0)$ of a single Abelian mode with rapidity wave number $\nu = 10.053$. The solid line is the semianalytic result of Ref. [34] and the dot-dashed lines are the results obtained from our 1 + 1 numerical solutions using two different methods (A and B) for discretizing the shifted momentum-space rapidity $\bar{y} = y - \eta$. The inset shows relative error of the two methods. The run was made using $\tau_{\rm iso} = 0.1$, $\tau_0 = 1.0$, $m_D = 10$, $a = 0.0025$, $\epsilon = 0.001$, $N_\eta = 250$, $N_\phi = 8$, and $N_y = 1000$ (method A), $N_x = 1000$ (method B).

in an earlier work [34] where, for the Abelian case, the equations of motion for the $\mathcal{W}$ field have been solved in terms of integro-differential equations. Figure 1 compares a semianalytic result obtained from the latter with results obtained using the two different methods of discretization described above and detailed in Appendixes A and B. As can be seen from this figure both numerical discretizations reliably reproduce the Abelian semianalytic result. In the inset we compare the relative error defined as the difference of the time evolution obtained from method A or B with the semianalytic result over the sum (relative percentage error). As can be seen from this inset, method B seems to perform better at late times, so unless otherwise indicated, all final results presented will be using method B. However, in practice, we have made runs comparing the predictions of methods A and B in all cases and find that there is very little difference between the results obtained with the two methods.

B. Single-mode results

In Fig. 2 we show results of a simulation of a single SU(2) mode with rapidity wave number $\nu = 10.053$ (same mode as Fig. 1 but now also with the color direction rotating with period $2\pi/\nu$ in space-time rapidity η). In Fig. 2(a) we show the proper-time evolution of the magnetic, electric, and total field energy densities in units where $\tau_0 = 1$ and, following Ref. [36], scaled with a factor of τ. Because the energy in the hard particles is dropping proportionally to τ^{-1}, this corresponds to giving the various soft energy densities in terms of the hard energy density (times a parametrically small number $\sim g^2$ since the hard energy density is assumed to be much larger than the soft ones in order that the hard-loop approximation be applicable.)

The various components of the (soft) field energy density are defined by

$$\begin{aligned}\mathcal{E} &= \mathcal{E}_T + \mathcal{E}_L = \mathcal{E}_{B_T} + \mathcal{E}_{E_T} + \mathcal{E}_{B_L} + \mathcal{E}_{E_L} \\ &= \mathrm{tr}[\tau^{-2}F_{\eta i}^2 + \tau^{-2}\Pi_i^2 + F_{xy}^2 + (\Pi^\eta)^2]. \end{aligned} \tag{38}$$

Because of the expansion of the system, the total energy density $\mathcal{E}$ is not conserved, even when the induced current (25) is identically zero. In this case the time dependence is governed by the fact that the Hamiltonian density [36] $\mathcal{H} = \tau\mathcal{E}$ satisfies

$$\frac{d}{d\tau}\mathcal{H} = \frac{\partial}{\partial\tau}\mathcal{H} = \mathcal{E}_L - \mathcal{E}_T, \tag{39}$$

and therefore

$$\frac{d}{d\tau}\mathcal{E}|_{j\equiv 0} = -\frac{2}{\tau}\mathcal{E}_T|_{j\equiv 0}. \tag{40}$$

In the presence of a plasma of hard particles and thus nonvanishing induced current j, we define the net energy gain rate by

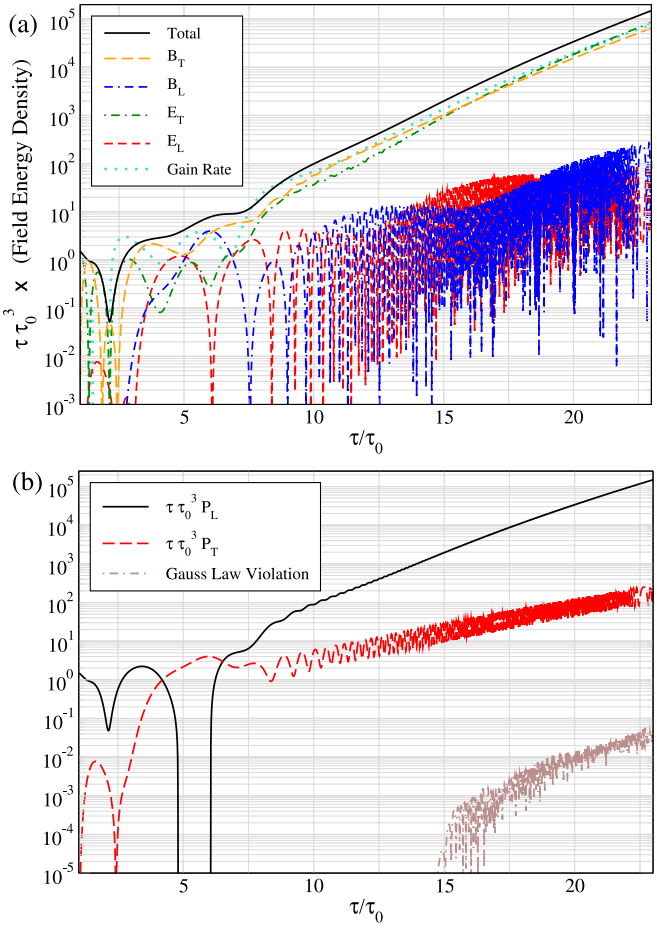

FIG. 2 (color online). Results from a run with a single non-Abelian mode with $\nu = 10.053$. In the top panel (a) we show the proper-time dependence of the chromofield energy densities. In the lower panel (b) we show the longitudinal and transverse pressures along with our numerical Gauss law violation. The run was made using $\tau_{\mathrm{iso}} = 0.1$, $\tau_0 = 1.0$, $m_D = 10$, $a = 0.0025$, $\epsilon = 0.001$, $N_\eta = 500$, $N_x = 100$, and $N_\phi = 100$.

$$R_{\text{Energy Gain}} \equiv \frac{d\mathcal{E}}{d\tau} + \frac{2}{\tau}\mathcal{E}_T, \tag{41}$$

which in the plots showing the energy densities is included as the dotted line marked "Gain Rate." The latter gives the rate of energy transfer from the free-streaming hard particles into the collective chromofields. As can be seen from Fig. 2, for SU(2) the single-mode evolution is quite complicated with all field components being dynamically generated; however, at late times transverse chromoelectric and chromomagnetic fields exponentially dominate.

In Fig. 2(b) we plot the longitudinal and transverse field pressures generated during the system's dynamical evolution. These are obtained from [36]

$$P_L = \mathcal{E}_T - \mathcal{E}_L, \qquad P_T = \mathcal{E}_L, \tag{42}$$

where as before $\mathcal{E}_T$ is the sum of the energy density coming from transverse electric and magnetic fields and $\mathcal{E}_L$ is the

sum of the energy density coming from longitudinal electric and magnetic fields. As shown in Fig. 2(b) the system generates both longitudinal and transverse pressures. At short times ($\tau/\tau_0 \sim 5$–6) for this single-mode evolution we find that the longitudinal pressure becomes momentarily negative; however, at late times the effect of the chromofield instability is to generate exponentially large longitudinal field pressure, whereas the longitudinal pressure of the (free-streaming) particles drops according to $\tau P_L^{\text{part.}} \sim \tau^{-2}$.

Also shown in Fig. 2(b) is our measure of violation of Gauss law which is determined by evaluating the τ component of the equations of motion as detailed in Eqs. (36) and (A13). As can be seen from this figure, although our violation of the Gauss law constraint grows with time, it is numerically under control and always orders of magnitude below the field energy density. The amount of violation can be systematically reduced by taking finer lattices in η and velocity space. We have found that our results for the time evolution of the energy densities, pressures, etc. remain the same as our numerical Gauss law violation is reduced further, giving us confidence in our algorithm. As a general rule we always terminate our runs when the Gauss law violation becomes of order 1.

For comparison, in Fig. 3 we show the evolution of the field energy densities in the case of pure Yang-Mills evolution. This is obtained by decoupling the free-streaming particle currents by setting j^α to zero in the field equations of motion. From Fig. 3(a) we see that in the case of pure Yang-Mills evolution the field energy density decreases over the entire time interval shown. The "Gain Rate" control variable is approximately zero and shows the level of discretization errors. In addition we see that although both longitudinal and transverse pressures are generated they are of much smaller magnitude than those generated when the free-streaming particle currents are coupled into the Yang-Mills equations. Therefore, we have demonstrated that coupling in the particle currents generates qualitatively different field dynamics.

C. Initial non-Abelian noise and partial Abelianization

In Fig. 4 we show results obtained from an SU(2) non-Abelian run in which the initial condition is taken to be a random superposition of discrete transverse electric field modes (both Π_x and Π_y) with an ultraviolet cutoff $\Lambda_\nu = 20$ in space-time rapidity wave number ν. The amplitude for each mode is chosen from a Gaussian probability distribution centered at zero with standard deviation $\sigma = 0.03$. As can be seen from Fig. 4(a) the system very quickly generates chromomagnetic fields, whereas during the early times energy is equally distributed between transverse chromoelectric and chromomagnetic fields. Longitudinal field energies which vanish initially grow exponentially with a rate about twice that of the transverse fields, but almost saturate when the nonlinear regime is reached. During the initial growth phase as well as in the deep nonlinear regime, the energy density is exponentially dominated by transverse chromomagnetic fields. This again translates into the generation of exponentially large longitudinal pressure as shown in Fig. 4(b).

In Fig. 4(c) we plot various measures of the Abelianization and (color) correlations of the chromofields. Following Refs. [29,31] we define a measure of the "Abelianness" of the field configurations through

$$\bar{C}[j] = \int_0^{L_\eta} \frac{d\eta}{L_\eta} \frac{\{\mathrm{tr}((i[j_x, j_y])^2)\}^{1/2}}{\mathrm{tr}(j_x^2 + j_y^2)}. \tag{43}$$

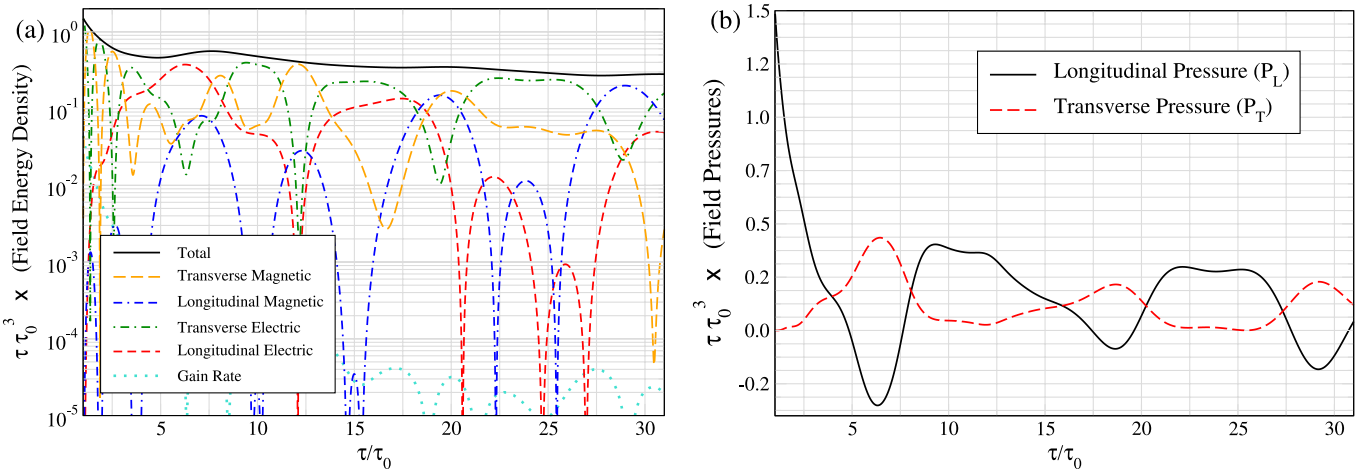

FIG. 3 (color online). Results from a run with a single non-Abelian mode with rapidity wave number $\nu = 10.053$ in which we have decoupled the hard particle currents ($j = 0$) so that we are simply solving the Yang-Mills equations in the expanding metric. In the left panel (a) we show the proper-time dependence of the chromofield energy densities. In the right panel (b) we show the longitudinal and transverse pressures. Gauss law is obeyed exactly by our algorithm in this case. The run was made using $\tau_{\text{iso}} = 0.1$, $\tau_0 = 1.0$, $m_D = 10$, $a = 0.0025$, $\epsilon = 0.001$, and $N_\eta = 500$.

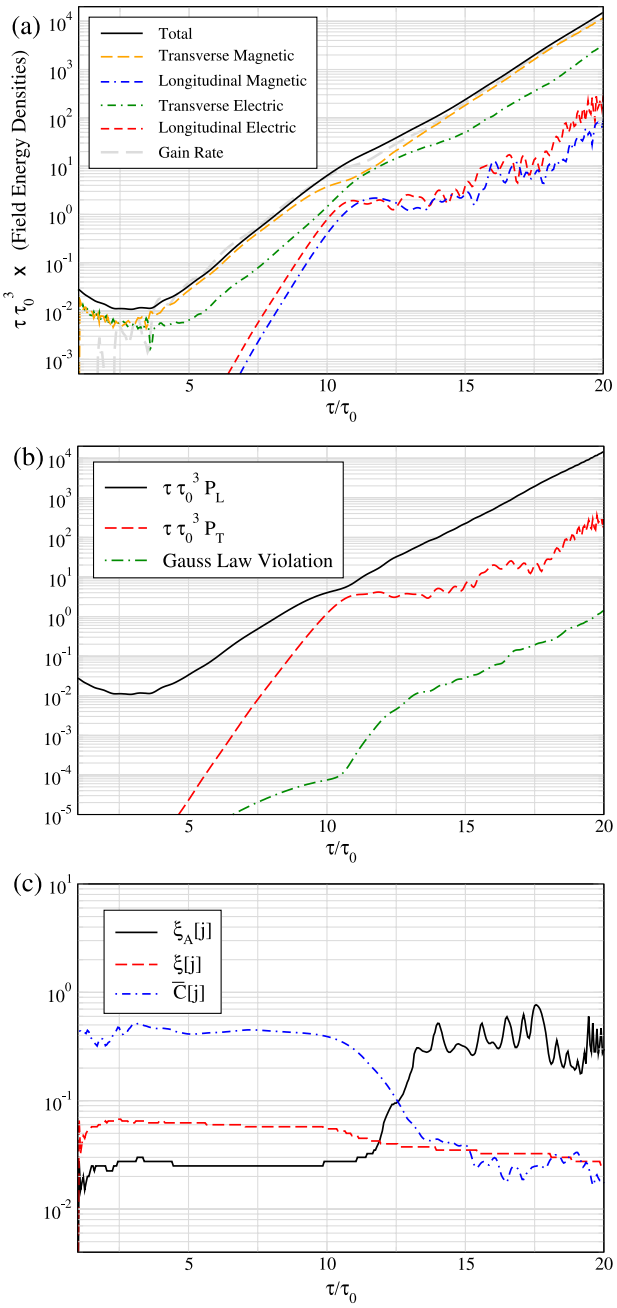

FIG. 4 (color online). Results from a non-Abelian run initialized with a random superposition of discrete electric modes (cutoff white noise). In the top panel (a) we show the proper-time dependence of the chromofield energy densities and the energy gain rate (41) times an extra factor of τ_0. In the middle panel (b) we show the longitudinal and transverse pressures along with our numerical Gauss law violation. In the bottom panel (c) we show the correlations $\xi_A[j]$, $\xi[j]$, and $\bar{C}[j]$. The run was made using $\tau_{\rm iso} = 0.1$, $\tau_0 = 1.0$, $m_D = 10$, $\sigma = 0.03$, $\Lambda_\nu = 20$, $a = 0.0025$, $\epsilon = 0.000\,25$, $N_\eta = 1000$, $N_x = 100$, and $N_\phi = 100$.

If the field configurations are Abelian (aligned in one color direction) then this quantity vanishes because of the commutator in the numerator.

In order to further study the color correlations of the chromofields in spatial rapidity, η, we define

$$\chi_A(\xi) = \frac{N_c^2 - 1}{2N_c} \int_0^{L_\eta} \frac{d\eta}{L_\eta} \times \frac{\mathrm{tr}\{(i[j_i(\eta+\xi), \mathcal{U}(\eta+\xi,\eta) j_j(\eta)])^2\}}{\mathrm{tr}\{j_k^2(\eta+\xi)\}\mathrm{tr}\{j_l^2(\eta)\}}, \quad (44)$$

where $\mathcal{U}(\eta', \eta)$ is the adjoint-representation parallel transport from η to η'. When colors are completely uncorrelated over a distance ξ, this quantity equals unity; if they point in the same direction, this quantity vanishes. Following Refs. [29,31] we define the "Abelianization correlation length" ξ_A as the smallest distance where χ_A is larger than $1/2$,

$$\xi_A[j] = \min_{\chi_A(\xi) \geq 1/2} (\xi). \quad (45)$$

This we compare with a general correlation length, which does not focus on color, defined through the gauge-invariant function

$$\chi(\xi) = \frac{\int_0^{L_\eta} d\eta \mathrm{tr}\{j_i(\eta+\xi)\mathcal{U}(\eta+\xi,\eta) j_i(\eta)\}}{\int_0^{L_\eta} d\eta \mathrm{tr}\{j_l(\eta) j_l(\eta)\}}. \quad (46)$$

This function now vanishes when fields are uncorrelated over a distance ξ, and it is normalized such that $\chi(0) = 1$. We thus define the general correlation length through

$$\xi[j] = \min_{\chi(\xi) \leq 1/2} (\xi). \quad (47)$$

Figure 4(c) shows that the system becomes Abelianized with large color correlation length, $\xi_A[j]$, when the fields have grown such that nonlinear self-interactions become important. ξ_A occasionally even shoots up to the size of the space-time rapidity lattice (2.5 in this case) before settling to oscillations around rapidities $\sim$0.3. (The indication of some late-time growth of ξ_A is presumably spurious, since it is accompanied by the onset of a rapid growth of the Gauss law violation control parameter.) Although we show the output of only one run here, the behavior shown is generic for all random seeds we have studied.

D. Color-glass-condensate-inspired initial conditions

In Fig. 5 we show results obtained by using initial seed fields which reflect the spectral properties obtained by Fukushima, Gelis, and McLerran (FGM) within the color-glass-condensate (CGC) framework [54]. We use again a random superposition of modes, but now involving already initially both chromoelectric and chromomagnetic transverse fields with a spectrum[7]

[7]The spectrum of fluctuation derived in Ref. [54] of course also has modes which are not constant in the transverse coordinates, but in our present framework we have to restrict ourselves to modes which are effectively 1 + 1 dimensional.

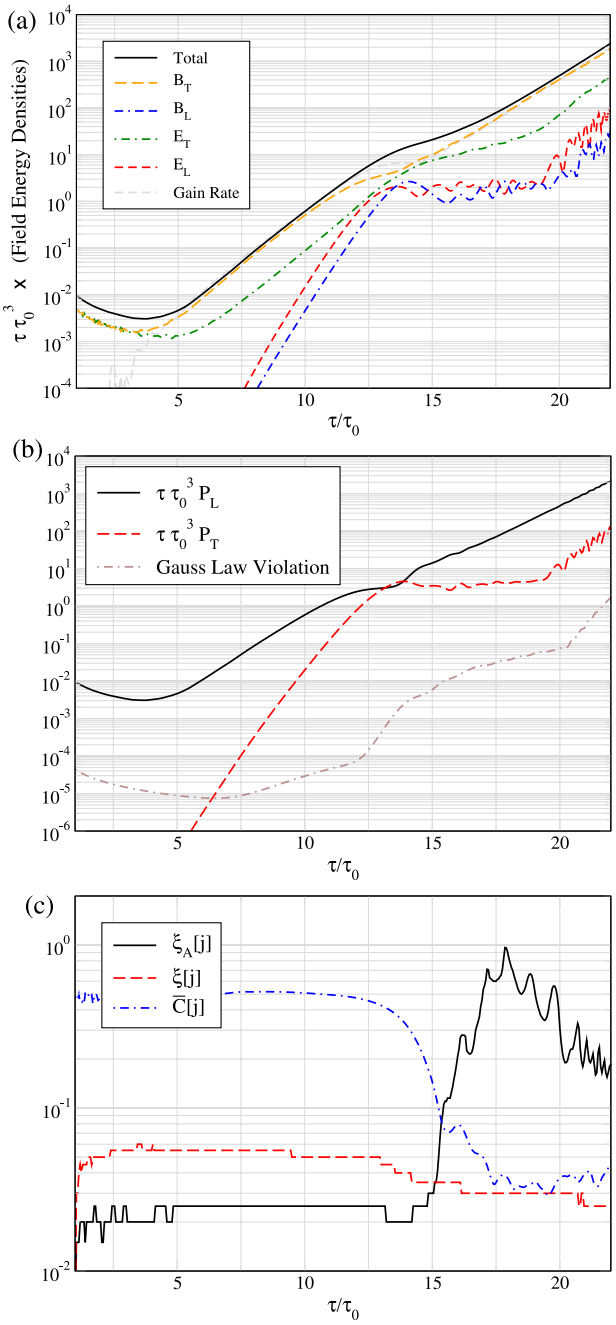

FIG. 5 (color online). Results from non-Abelian run initialized with FGM initial conditions. In the top panel (a) we show the proper-time dependence of the chromofield energy densities and the energy gain rate (41) times an extra factor of τ_0. In the middle panel (b) we show the longitudinal and transverse pressures along with our numerical Gauss law violation. In the bottom panel (c) we show the correlations $\xi_A[j]$, $\xi[j]$, and $\bar{C}[j]$. The run was made using $\tau_{\rm iso} = 0.1$, $\tau_0 = 1.0$, $m_D = 10$, $\sigma = 0.05$, $\Lambda_\nu = 20$, $a = 0.005$, $\epsilon = 0.0005$, $N_\eta = 500$, $N_x = 200$, and $N_\phi = 200$.

$$|\,\Pi_i(\nu)|_{\tau=\tau_0} = \sigma\sqrt{\nu}, \qquad |\,A^i(\nu)|_{\tau=\tau_0} = \sigma/\sqrt{\nu}, \quad (48)$$

for all space-time rapidity wave numbers $\nu \le \Lambda_\nu$ that are allowed by the periodic boundary conditions of our finite η lattice, excluding, however, $\nu = 0$. The phases of each color component of these modes is taken at random, and we have used a small value $\sigma = 0.05$, corresponding to initially weak fields. In accordance with Ref. [54], the longitudinal magnetic field is set to zero initially through $A_\eta|_{\tau=\tau_0} = 0$, but the non-Abelian Gauss law leads to nonvanishing longitudinal chromoelectric fields even though $j^\tau \equiv 0$ initially.

With $A_\eta = 0$ initially, the Gauss law constraint in the 1 + 1-dimensional setting gives

$$\partial_\eta \Pi^\eta = ig[A^i, \Pi_i]. \quad (49)$$

Having populated the transverse field modes according to Eq. (48), we solve the lattice version of Eq. (49) to determine the longitudinal electric field $E^i = \Pi^i/\tau$.

However, in contrast to the simpler initial conditions used above, this presents a problem with the periodicity of our η lattice, since the solution thus obtained does not share the periodicity of all other fields, leading to a Gauss law violation at the boundary in the form of a mismatch of Π^η. This initially small violation, however, quickly grows and cannot be tolerated. We have solved this problem by singling out the lowest lying mode of A^x and calculating its contribution to the mismatch of Π^η. By elementary linear algebra we determine how to rescale the color components of this one mode such that the mismatch is eliminated, but this rescaling is only accepted when the total amplitude of this mode does not get modified by more than 50%. If this is not the case, a different set of random numbers for the phases of all transverse color fields is generated and the procedure repeated until a configuration is found where the amplitude of the lowest lying mode of A_x is not too far from the starting point (48).

The results shown in Fig. 5 are qualitatively similar to those obtained with an initial condition which is a random superposition of purely electric modes. As can be seen from Fig. 5(a), at early times there is equal partitioning between chromoelectric and chromomagnetic fields which both initially decrease and then begin to grow exponentially with transverse chromomagnetic fields dominating for nearly the entire run. At $\tau/\tau_0 \sim 13$ there is a non-Abelian "bounce" when the longitudinal field components become on the same order of magnitude as the transverse ones; however, beyond this point in time the transverse field components again dominate. In Fig. 5(b) we see that the field pressures which are generated are also similar to those obtained with a random discrete Fourier spectrum with the system generating an exponentially large longitudinal pressure due to the chromo-Weibel instability. In Fig. 5(c) the behavior of the Abelianization measure, $\bar{C}[j]$, and correlation lengths are again similar to the random discrete Fourier spectrum initial conditions, showing an Abelianization of the fields and large color correlation length at late times. This demonstrates that the qualitative

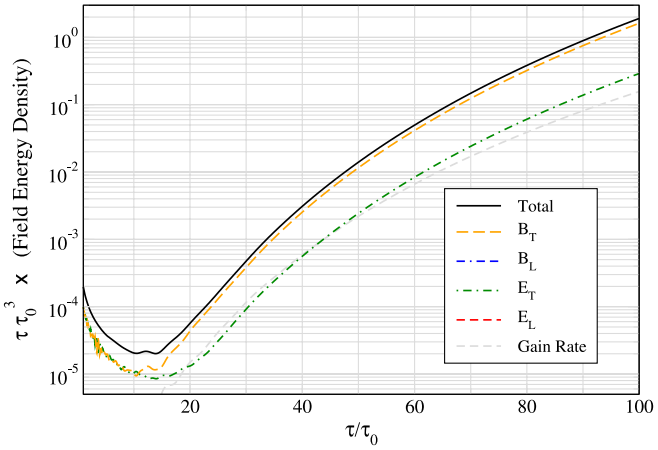

FIG. 6 (color online). Field energy density results from an Abelian run initialized with FGM initial conditions. Transverse fields and Gauss law violation are zero to within machine precision. The field pressure is purely longitudinal and coincides with the total field energy density. The run was made using $\tau_{\rm iso} = 0.1$, $\tau_0 = 1.0$, $m_D = 3.585$, $\sigma = 0.017\,32$, $\Lambda_\nu = 20$, $a = 0.01$, $\epsilon = 0.001$, $N_\eta = 500$, $N_x = 100$, and $N_\phi = 4$.

features of the time evolution of the instability induced fields are independent of the details of the initial condition.[8]

In Figs. 6 and 7 we show results obtained using FGM initial conditions with a smaller Debye mass corresponding to the estimates of the "gluon liberation factor" c obtained from the color-glass-condensate picture [55,56] (see Appendix C for details). In Fig. 6 we show the results obtained from an Abelian run in which all fields were constrained to initially point in the same direction in color space, and in Fig. 7 we show the results of a non-Abelian SU(2) run. As can be seen from both figures the primary effect of lowering m_D is to slow down the growth of the chromofields; however, besides this "stretching" of the time axis there is little qualitative difference between the larger m_D run (Fig. 5) and this case, Fig. 7. We still observe domination by transverse chromofields, which now have larger color correlation length, and generate exponentially large longitudinal pressure.

In Fig. 8 we compare six different non-Abelian SU(2) runs with FGM initial conditions in which we have taken different values for the spectral cutoff in rapidity wave number, Λ_ν, imposed on the FGM initial condition. As can be seen from this figure for fixed initial energy density the effect of increasing Λ_ν is to delay the onset of exponential growth of the chromofields. This is to be expected since for fixed energy density the occupation number of the lowest ν modes must be decreased as Λ_ν is increased, and

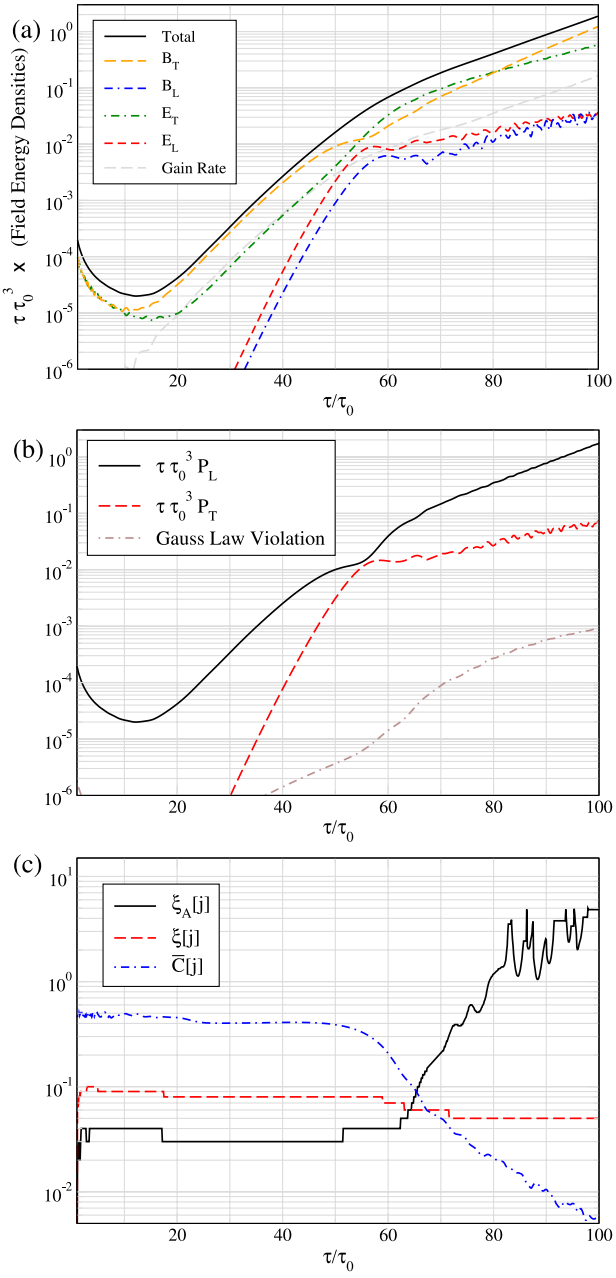

FIG. 7 (color online). Results from a non-Abelian run initialized with FGM initial conditions. In the top panel (a) we show the proper-time dependence of the chromofield energy densities and the energy gain rate (41) times an extra factor of τ_0. In the middle panel (b) we show the longitudinal and transverse pressures along with our numerical Gauss law violation. In the bottom panel (c) we show the correlations $\xi_A[j]$, $\xi[j]$, and $\bar{C}[j]$. The run was made using $\tau_{\rm iso} = 0.1$, $\tau_0 = 1.0$, $m_D = 3.585$, $\sigma = 0.01$, $\Lambda_\nu = 20$, $a = 0.01$, $\epsilon = 0.001$, $N_\eta = 500$, $N_x = 200$, and $N_\phi = 100$.

higher modes have a larger delay, as already found in the Abelian case studied in Ref. [34]. In fact, the amplitude of the low-momentum modes must be decreased rapidly since the high-momentum modes dominate the energy density. In Fig. 8(b) we show a fit to the "time to return," τ_R, of the

[8]Of course, by this we mean any reasonable initial condition. Choosing, for example, an initial condition which only had very high frequency modes would greatly delay the onset of instability-driven growth of the fields.

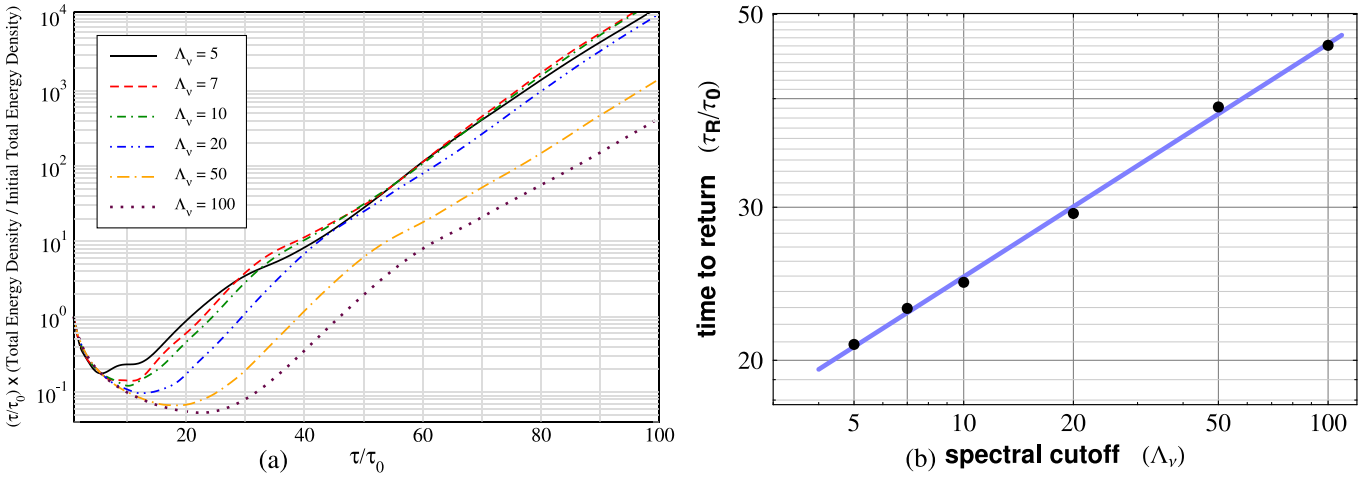

FIG. 8 (color online). The left panel (a) shows the total field energy density results from a non-Abelian run initialized with FGM initial conditions and different UV cutoffs, $\Lambda_\nu \in \{5, 7, 10, 20, 50, 100\}$, imposed on the initial spectrum. The right panel (b) shows the "time to return" τ_R/τ_0, defined as the point at which the field energy density has returned to its initial value, as a function of the FGM spectral cutoff Λ_ν on a log-log plot. The blue line (right panel) shows a fit to a power law $\tau_R = a\tau_0(\Lambda_\nu)^b$. Runs were made using $\tau_{\rm iso} = 0.1$, $\tau_0 = 1.0$, $m_D = 3.585$, $\sigma = 0.06$, $a = 0.005$, $\epsilon = 0.0025$, $N_\eta = 1000$, $N_y = 800$, and $N_\phi = 50$. For this figure discretization method A was used.

scaled energy density $\tau\tau_0^3\mathcal{E}$, i.e. the time it takes the instability to compensate for the initial decay of the soft fields caused by the system's expansion. Fitting this time (in units of τ_0) by a power-law $a(\Lambda_\nu)^b$, we find $a = 13.46 \pm 0.01$ and $b = 0.26 \pm 0.01$. The exponent b is consistent with being $1/4$. The coefficient a depends on the Debye mass and decreases as m_D increases.

In Fig. 9 we compare the rapidity (ν) spectrum obtained by Fourier transforming the trace of the conjugate field momenta, $\mathrm{tr}(\mathbf{\Pi}^2) = \mathrm{tr}(\Pi_i^2 + \tau^2(\Pi^\eta)^2)$, in order to gain more understanding of the momentum-space dynamics of the fields in our simulations. In Fig. 9(a) we show the spectrum resulting from analysis of the induced current from the Abelian run shown in Fig. 6. In Fig. 9(b) we show the spectrum resulting from analysis of the induced current from the non-Abelian run shown in Fig. 7. The lowest (bold green) line indicates the starting spectrum, the middle (bold blue) line indicates the "non-Abelian point" at which all field components become approximately equal in magnitude, and the uppermost (bold red) line shows the final spectrum obtained in our simulations. As can be seen from this figure there is a stark qualitative difference between the Abelian and non-Abelian spectra, with the former maintaining the spectral cutoff imposed on the initial condition and the latter "cascading" energy to higher and higher momentum modes starting already at

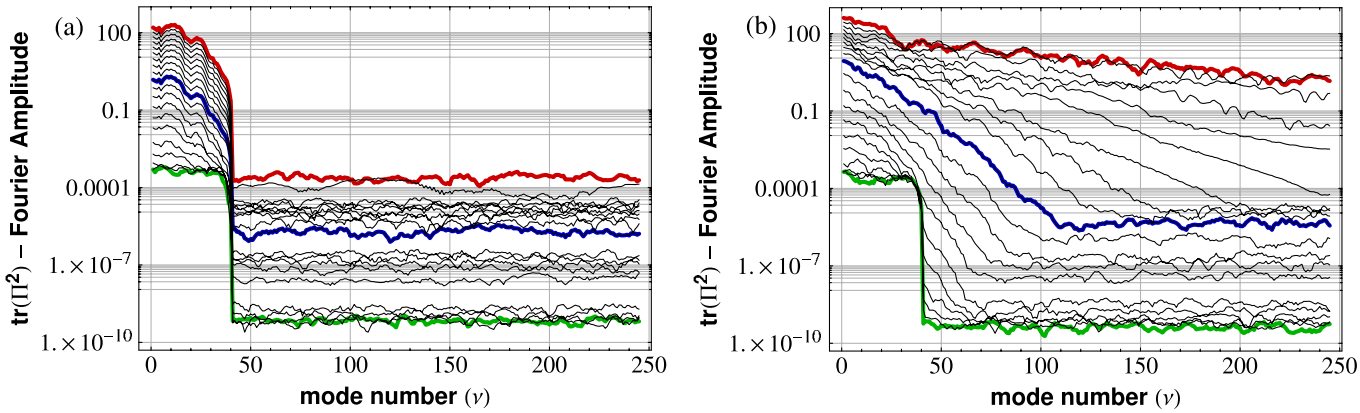

FIG. 9 (color online). Fourier spectrum of the color-traced conjugate field momenta, $\mathrm{tr}(\mathbf{\Pi}^2)$, obtained from Abelian (left panel) and non-Abelian (right panel) runs with FGM initial conditions. The lowest (bold green) line indicates the starting spectrum and the uppermost (bold red) line indicates the final spectrum. In the right panel the bold blue line indicates the "non-Abelian point" at $\tau/\tau_0 \sim 55$ when all field components become approximately the same order of magnitude. The Abelian and non-Abelian spectra were obtained by analyzing the currents produced during the runs shown in Figs. 6 and 7, respectively.

very early times. This is similar to earlier results for the spectra induced by instability growth [15]. Surprisingly, in Fig. 9(b) one sees that at the "non-Abelian point" indicated by the bold blue line the low frequency modes have generated a quasithermal (Boltzmann) distribution up to $\nu \sim 80$. In fact, the development of the quasithermal distribution begins at very early times, and one can associate a temperature with the system by fitting the low-ν spectra with exponential fits from rather early times. Similar spectra are generated when one measures $\mathrm{tr}(\mathbf{A}^2)$, which also allows one to define a kind of magnetic temperature from that observable as well.

IV. DISCUSSION, CONCLUSIONS, AND OUTLOOK

In this paper we have performed the first numerical study of non-Abelian plasma instabilities in a nonstationary, longitudinally expanding system within the framework of discretized hard-loop theory,[9] extending the semianalytical results of [34] for the weak-field, Abelian regime. We have worked out the case of the most unstable modes which are constant modes in the transverse direction, making the dynamics 1 + 1 dimensional in configuration space (while momentum space remains three dimensional). Starting with only small rapidity fluctuations, we found that the exponential (in $\sqrt{\tau}$ [34]) growth in the Abelian (weak-field) phase is only mildly weakened when nonlinearities through non-Abelian self-interactions of the collective fields set in, and this is associated with a significant degree of Abelianization in finite domains in the nonlinear regime. This is quite similar to what was observed in the 1D + 3V simulations in a stationary anisotropic plasma [24], and it remains to be seen what full 3D + 3V simulations will give. However, it is quite plausible that the 1D + 3V results already capture the behavior of the more generic 3D + 3V simulations, because it was recently observed [33] that for extreme anisotropies a saturation of the growth as was found in Refs. [30,31] at moderate anisotropies will occur only at correspondingly extreme values of the fields, if at all. Indeed, our simulations start out with strong anisotropy of the particle distribution, which rapidly grows with increasing time according to Eq. (19).

In our simulations we have found that in the non-Abelian case the growing unstable modes tend towards a quasithermal spectrum [Fig. 9(b)] and they produce mainly longitudinal field pressure, which grows exponentially, thereby realizing a bottom-up isotropization scenario in which the soft modes make up for the strongly decaying longitudinal particle pressure, which goes like $1/\tau^3$. The transverse particle pressure, which according to the CGC picture is approximately thermal by itself, is decaying like $1/\tau$. In the hard-expanding-loop theory which we have considered, we can of course only trust the beginning of this scenario, since the backreaction of the collective fields on the hard particle background is neglected, and it is in fact the reservoir of energy in the hard particle background that is feeding the growth of the soft modes, which has to stop before the energy in the latter becomes comparable with the former.

In Fig. 10(a) we have reproduced the results of Fig. 7(b) for the field pressures obtained by choosing dimensionful parameters motivated by the CGC scenario as described in Appendix C and compared also with the particle pressures that follow from this matching. Notice that all quantities are multiplied by τ so that the decaying transverse particle

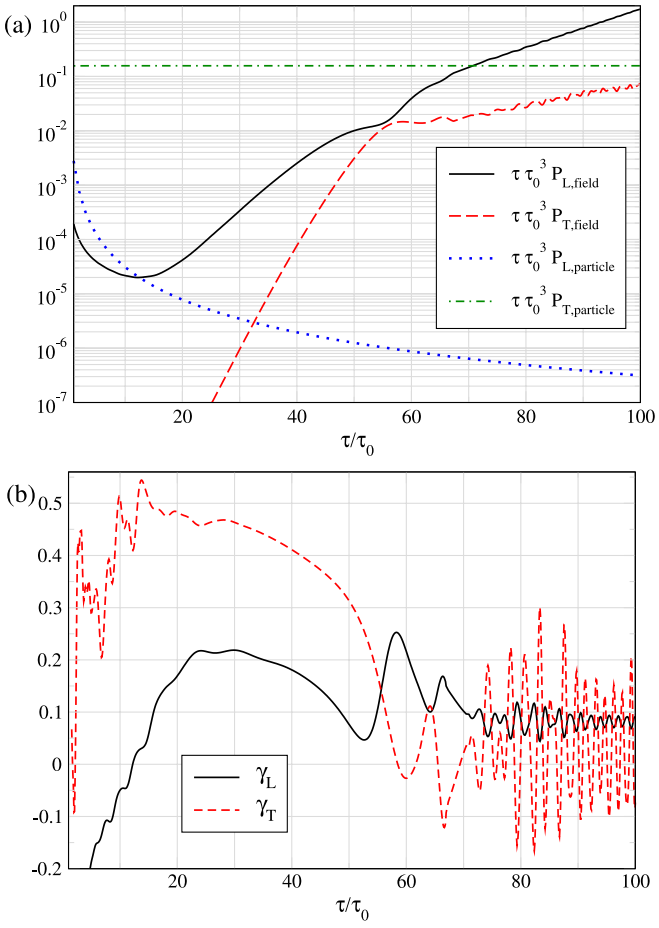

FIG. 10 (color online). The top panel (a) shows a comparison of particle and field pressures generated during a typical run which uses CGC-inspired "FGM" initial conditions. Simulation parameters are the same as shown in Fig. 7 and the field pressures are the same as in panel (b) of that figure. The particle pressures are obtained by evaluating the expressions given in Eqs. (16) and (17). In order to fix the initial energy densities, we use the scheme detailed in Appendix C assuming $\alpha_s = 0.3$, which gives $\mathcal{E}(\tau_0) \simeq 0.3 Q_s^4$. In the lower panel (b) we show the growth rates for the field pressures in units of τ_0^{-1}.

[9]Closely related instabilities have been found before numerically in the color-glass condensate framework in Refs. [35,36], where the role of plasma particles is played by high-momentum modes of the Yang-Mills field.

pressure is represented by an approximately horizontal line.

The time scale $\tau_0 \simeq Q_s^{-1}$ can be roughly identified with 1–1.5 and 3 GeV for RHIC and LHC experiments, respectively, where the plasma lifetimes are probably less than 5 fm/c $\simeq 25$–$35\tau_0$ for RHIC, and probably much larger than 7 fm/c $\simeq 100\tau_0$ for the LHC [57]. Defining an effective growth rate of the longitudinal pressure by

$$\gamma_L = \frac{\partial}{\partial \tau} \ln(\tau \tau_0^3 P_{L,\mathrm{field}}), \tag{50}$$

we find for the example provided in Fig. 10 a maximal value of about $\gamma_L \sim 0.2\tau_0^{-1}$ in the weak-field regime for $\tau \gtrsim 20\tau_0$, and about $0.1\tau_0^{-1}$ in the strong-field (non-Abelian) regime $\tau \gtrsim 70\tau_0$. This corresponds to minimum characteristic time scales of

$$\min \gamma_L^{-1} \sim \begin{cases} 0.7 - 1 \text{ fm/c} & \text{(RHIC)} \\ 0.3 \text{ fm/c} & \text{(LHC)} \end{cases} \tag{51}$$

in the weak-field regime, and twice that in the strong-field regime. This agrees roughly with the preisotropization values obtained in Ref. [42] from classical-statistical lattice gauge theory.[10]

However, at least for the case of initially small rapidity fluctuations which we have considered here, there is a delay of the onset of plasma instabilities caused by the expansion which appears uncomfortably large for RHIC energies, even if one chooses smaller spectral cutoffs in the initial fluctuations which somewhat reduce this delay (cf. Fig. 8).

Still, for the LHC our results suggest that plasma instabilities like those studied here will be an important phenomenon, in particular if LHC energies make contact to a more weakly coupled quark-gluon plasma as suggested for instance by the analysis of Ref. [58]. The comparison of particle and field pressure in Fig. 10(a) indicates upper limits for an isotropization point, which are, however, strongly dependent on the initial strength of the rapidity fluctuations. Larger seed fields will correspondingly lower this point. However, experience from simulations of non-Abelian plasma instabilities in the stationary anisotropic case [30,31,33] lets us expect that full 3D + 3V studies (or at least 2D + 3V ones [38]) are required to analyze truly strong initial fields. This will be the subject of follow-up work.

ACKNOWLEDGMENTS

We thank Peter Arnold, Jürgen Berges, Paul Romatschke, Kari Rummukainen, and Christof Wetterich for useful conversations and feedback. M. S. was supported by DFG Project No. GR 1536/6-1 and the Kavli Institute for Theoretical Physics NSF Grant No. PHY05-51164; A. R. and M. A. acknowledge support by FWF Project No. P19526. M. S. and M. A. also acknowledge support during the Galileo Galilei Institute for Theoretical Physics program on High Density QCD.

APPENDIX A: LATTICE DISCRETIZATION METHOD A

The one-dimensional situation studied herein assumes that fields vary only in the η direction. We then have transverse adjoint-scalar fields A^i with $i = 1, 2$ and auxiliary fields $\mathcal{W}_{\phi,\bar{y}}$ which all are defined on the sites s of a periodic spatial rapidity lattice with (dimensionless) lattice spacing a. The conjugate momenta Π_i live on the temporal links, while the conjugate momentum Π^η of the gauge field A_η, which appears only in the form of a parallel transporter $U_{s+(1/2)} = \exp(igaA_{\eta,s})$, will be treated as located on the timelike plaquette on top of the link between site s and $s + 1$.

Apart from U, all of these fields are represented by $N_c \times N_c$ traceless Hermitian matrices which for SU(2) reduce to the 2×2 Pauli matrices. Although we are going to make explicit all occurrences of the coupling g, in practice we have taken $g = 1$ through a rescaling of the fields.

Covariant derivatives are defined in three versions: left and right covariant,

$$\begin{aligned} D_\eta^R A_s^\alpha &\equiv \frac{A_s^\alpha - U_{s-(1/2)} A_{s-1}^\alpha U_{s-(1/2)}^\dagger}{a}, \\ D_\eta^L A_s^\alpha &\equiv \frac{U_{s+(1/2)}^\dagger A_{s+1}^\alpha U_{s+(1/2)} - A_s^\alpha}{a}, \end{aligned} \tag{A1}$$

and symmetric,

$$D_\eta^S \equiv (D_\eta^L + D_\eta^R)/2. \tag{A2}$$

The second order is given by

$$D_\eta^2 \equiv (D_\eta^L - D_\eta^R)/a \tag{A3}$$

and is automatically symmetric.

In method A, the auxiliary field $\mathcal{W}(\tau, \eta; \phi, y)$ of the continuum theory is modeled by a large number of fields $\mathcal{W}_{s;\phi,\bar{y}}$ with $\bar{y} = y - \eta$ discretized with $N_{\bar{y}}$ points in the interval $(-\Lambda_{\bar{y}}, \Lambda_{\bar{y}})$ and N_ϕ points for $0 \le \phi < 2\pi$. Additionally, we can absorb all or part of the denominator appearing in Eq. (25) for the induced current by writing

$$\bar{\mathcal{W}}_{s;\phi,\bar{y}}(\tau) = f^{-1}(\tau, \bar{y}) \mathcal{W}_{s;\phi,\bar{y}}(\tau) \tag{A4}$$

with

[10]The higher growth rate of the transverse field pressure, which is due to non-Abelian self-interactions of the chromofields (it vanishes in the Abelian case), is what Ref. [42] would call a "secondary" instability.

$$f(\tau,\bar{y}) = \left(1 + \frac{\tau^2}{\tau_{\rm iso}^2}\sinh^2(\bar{y})\right)^{\lambda}, \tag{A5}$$

with λ a number between 0 and 2. This does not produce extra terms in the equation of motion for $\bar{\mathcal{W}}$ because

$$\left[\partial_\tau + \frac{\tanh(\bar{y})}{\tau}\partial_\eta\right] f = 0. \tag{A6}$$

The induced current (25) is obtained from the auxiliary fields (which at $\tau = \tau_0 = 1$ are taken to vanish) according to

$$j_s^\alpha(\eta) = -\frac{m_D^2 \Lambda_{\bar{y}}}{N_\phi N_{\bar{y}}} \sum_\phi \sum_{\bar{y}} V^\alpha f^{\lambda-2} \bar{\mathcal{W}}_{s;\phi,\bar{y}}(\tau), \tag{A7}$$

with V^α defined in (11).

The equations of motion of the various fields are then solved numerically by a leapfrog procedure. The first step is to calculate the conjugate momenta from

$$\begin{aligned}
\Pi_{i,s}\left(\tau + \frac{\epsilon}{2}\right) &= \Pi_{i,s}\left(\tau - \frac{\epsilon}{2}\right) \\
&\quad + \epsilon\left(\tau j_s^i + \frac{1}{\tau} D_\eta^2 A_s^i + \tau g^2 i[A_s^j, i[A_s^j, A_s^i]]\right)_\tau, \\
\Pi_s^\eta\left(\tau + \frac{\epsilon}{2}\right) &= \Pi_s^\eta\left(\tau - \frac{\epsilon}{2}\right) \\
&\quad + \epsilon\left(-\frac{\tau}{2}(j_s^\eta + U_{s+(1/2)}^\dagger j_{s+1}^\eta U_{s+(1/2)}) \right. \\
&\quad \left. + \frac{ig}{\tau}[A_s^i, D_\eta^L A_s^i]\right)_\tau .
\end{aligned} \tag{A8}$$

The second step is to update the fields according to

$$A_s^i(\tau + \epsilon) = A_s^i(\tau) + \epsilon\left(\tau + \frac{\epsilon}{2}\right)^{-1} \Pi_{i,s}\left(\tau + \frac{\epsilon}{2}\right), \tag{A9}$$

$$\begin{aligned}
U_{s+(1/2)}(\tau + \epsilon) &= \exp\left(ig\epsilon a\left(\tau + \frac{\epsilon}{2}\right)\Pi_s^\eta\left(\tau + \frac{\epsilon}{2}\right)\right) \\
&\quad \times U_{s+(1/2)}(\tau),
\end{aligned} \tag{A10}$$

and the auxiliary fields $\bar{\mathcal{W}}$ according to

$$\begin{aligned}
\bar{\mathcal{W}}_{s;\phi,\bar{y}}(\tau + \epsilon) &= \bar{\mathcal{W}}_{s;\phi,\bar{y}}(\tau - \epsilon) + 2\epsilon\left\{f(\tau,\bar{y})^{-1}\mathcal{C} - g\frac{\mathcal{A}}{\cosh(\bar{y})} + \frac{\tanh(\bar{y})}{\tau}\right. \\
&\quad \left.\times\left[\left(1 - \frac{\tau^2}{\tau_{\rm iso}^2}\right) f(\tau,\bar{y})^{-1}\mathcal{B} - (D_\eta^S - \partial_{\bar{y}})\bar{\mathcal{W}}_{s;\phi,\bar{y}}(\tau)\right]\right\}
\end{aligned} \tag{A11}$$

with

$$\begin{aligned}
\mathcal{A} &\equiv i[v^i A_s^i(\tau), \bar{\mathcal{W}}_{s;\phi,\bar{y}}(\tau)], \\
\mathcal{B} &\equiv v^i D_\eta^S A_s^i(\tau), \\
\mathcal{C} &\equiv \left[\left(\tau + \frac{\epsilon}{2}\right)^{-1} v^i \Pi_{i,s}\left(\tau + \frac{\epsilon}{2}\right) + \left(\tau - \frac{\epsilon}{2}\right)^{-1} v^i \Pi_{i,s}\left(\tau - \frac{\epsilon}{2}\right)\right]/2 \\
&\quad - \frac{\sinh(\bar{y})}{4\tau_{\rm iso}^2}\left\{\left(\tau + \frac{\epsilon}{2}\right)^2\left[\Pi_s^\eta\left(\tau + \frac{\epsilon}{2}\right) + U_{s-(1/2)}\Pi_{s-1}^\eta\left(\tau + \frac{\epsilon}{2}\right)U_{s-(1/2)}^\dagger\right]\right. \\
&\quad \left. + \left(\tau - \frac{\epsilon}{2}\right)^2\left[\Pi_s^\eta\left(\tau - \frac{\epsilon}{2}\right) + U_{s-(1/2)}\Pi_{s-1}^\eta\left(\tau - \frac{\epsilon}{2}\right)U_{s-(1/2)}^\dagger\right]\right\}.
\end{aligned} \tag{A12}$$

The Gauss law constraint is checked by evaluating

$$\begin{aligned}
&\frac{1}{N_\eta}\sum_s {\rm tr}\left(\frac{1}{\tau} D_\eta^S \Pi_s^\eta\left(\tau + \frac{\epsilon}{2}\right)\right. \\
&\quad \left. - \frac{ig}{\tau}[A_s^i(\tau), \Pi_{i,s}\left(\tau + \frac{\epsilon}{2}\right)\right] - j^\tau(\tau)\Bigg)^2,
\end{aligned} \tag{A13}$$

and then taking a square root to obtain the results reported in the main body of the text.

APPENDIX B: LATTICE DISCRETIZATION METHOD B

In method B, the shifted momentum-space rapidity $\bar{y} = y - \eta$ is not discretized with uniform spacing in $\bar{y}$, but in a velocitylike variable x, $-1 < x < 1$, defined by

$$\bar{y} \equiv {\rm atanh}(x), \qquad d\bar{y} = \frac{1}{1 - x^2}\, dx. \tag{B1}$$

Compared to method A, this has the effect of giving more

lattice points around $\bar{y} = 0$, where the $\bar{\mathcal{W}}$ functions are typically sharply peaked.

With $\sinh^2(\bar{y}) = x^2/(1-x^2)$ and $\cosh^2(\bar{y}) = 1/(1-x^2)$, this leads to

$$\bar{\mathcal{W}}_{s;\phi,x}(\tau+\epsilon) = \bar{\mathcal{W}}_{s;\phi,x}(\tau-\epsilon) + 2\epsilon\Big(f(\tau,x)^{-1}\mathcal{C} - g(1-x^2)^{1/2}\mathcal{A} + \frac{x}{\tau}\Big[\Big(1-\frac{\tau^2}{\tau_{\rm iso}^2}\Big)f(\tau,x)^{-1}\mathcal{B} - (D_\eta^S - (1-x^2)\partial_x)\bar{\mathcal{W}}_{s;\phi,x}(\tau)\Big]\Big) \tag{B2}$$

with (choosing now $\lambda = 2$)

$$f(\tau,x) \equiv (1-x^2)^{-2}\Big(1+\Big(\frac{\tau^2}{\tau_{\rm iso}^2}-1\Big)x^2\Big)^2, \tag{B3}$$

and

$$\begin{aligned}
\mathcal{A} &\equiv i[v^i A_s^i(\tau), \bar{\mathcal{W}}_{s;\phi,x}(\tau)],\\
\mathcal{B} &\equiv v^i D_\eta^S A_s^i(\tau),\\
\mathcal{C} &\equiv \frac{v^i}{2\tau}\Big[\Pi_{i,s}\Big(\tau-\frac{\epsilon}{2}\Big)+\Pi_{i,s}\Big(\tau+\frac{\epsilon}{2}\Big)\Big] - \frac{\tau^2 x}{4\tau_{\rm iso}^2(1-x^2)^{1/2}}\Big[\Pi_s^\eta\Big(\tau-\frac{\epsilon}{2}\Big)+U_{s-(1/2)}\Pi_{s-1}^\eta\Big(\tau-\frac{\epsilon}{2}\Big)U_{s-(1/2)}^\dagger+\Pi_s^\eta\Big(\tau+\frac{\epsilon}{2}\Big)\\
&\quad + U_{s-(1/2)}\Pi_{s-1}^\eta\Big(\tau+\frac{\epsilon}{2}\Big)U_{s-(1/2)}^\dagger\Big].
\end{aligned} \tag{B4}$$

The currents are then given by

$$\begin{aligned}
j^\tau &= -m_D^2\int_0^{2\pi}d\phi\int_{-1}^1 dx(1-x^2)^{-(3/2)}\bar{\mathcal{W}},\\
j^i &= -m_D^2\int_0^{2\pi}d\phi\int_{-1}^1 dx v^i(1-x^2)^{-1}\bar{\mathcal{W}},\\
j^\eta &= -m_D^2\int_0^{2\pi}d\phi\int_{-1}^1 dx x(1-x^2)^{-(3/2)}\bar{\mathcal{W}},
\end{aligned} \tag{B5}$$

where the integrations over x and ϕ are replaced by uniformly spaced discrete sums.

All other lattice equations of motion are as in method A.

APPENDIX C: MATCHING TO CGC PARAMETERS

For fixing the dimensionful parameters of our numerical simulation in a way that makes contact with heavy-ion physics, we proceed as in Ref. [34] and refer to the color-glass-condensate framework [37,59] and take as the starting time for the plasma phase $\tau_0 \simeq Q_s^{-1}$, where Q_s is the so-called saturation scale.

In order to determine the only other dimensionful parameter in our HEL effective field equations, the Debye mass m_D at the (fictitious because of preplasma) time $t_{\rm iso}$, we assume a squashed Bose-Einstein distribution function for the hard particle distribution function (14) through $f_{\rm iso}(p) = \mathcal{N}(2N_g)/(e^{p/T}-1)$ where $N_g = N_c^2 - 1$ is the number of gluons and $\mathcal{N}$ a normalization that is adjusted such that at $\tau = \tau_0$ the hard-gluon density of CGC estimates is matched. Since the expansion is, by assumption, purely longitudinal, T is a constant transverse temperature, and it has indeed been found in CGC calculations that the gluon distribution is approximately thermal in the transverse directions, with $T = Q_s/d$ and $d^{-1} \simeq 0.47$ according to Ref. [37]. The normalization $\mathcal{N}$ can then be fixed by following Ref. [60], where the initial hard-gluon density is

$$n(\tau_0) = c\frac{N_g Q_s^3}{4\pi^2 N_c \alpha_s(Q_s\tau_0)}. \tag{C1}$$

Here c is the gluon liberation factor, for which different estimates can be extracted from the literature.

According to Ref. [60], the numerical CGC simulations of Refs. [61,62] correspond to $c \simeq 0.5$, while an approximate analytical calculation by Kovchegov [55] gave $c = 2\ln 2 \approx 1.386$. We adopted this higher value for the numerical simulations in Figs. 6–9, which is the more optimistic one from the point of view of plasma instabilities and which is actually not far from the most recent numerical result $c \simeq 1.1$ by Lappi [56].

With $\tau_{\rm iso}$ remaining a free parameter which determines how anisotropic the gluon distribution is at τ_0, the normalization $\mathcal{N}$ is now fixed by

$$n(\tau_0)\frac{\tau_0}{\tau_{\rm iso}} = n(\tau_{\rm iso}) = \frac{2\zeta(3)}{\pi^2}\mathcal{N}N_g T^3. \tag{C2}$$

For a purely gluonic plasma, the isotropic Debye mass is given by

$$m_D^2(\tau_{\rm iso}) = \mathcal{N}\frac{4\pi\alpha_s N_c T^2}{3}, \tag{C3}$$

which together leads to

$$m_D^2(\tau_{\rm iso})\tau_0^2(Q_s\tau_0)^{-1} = \frac{\pi c d}{6\zeta(3)}\frac{\tau_0}{\tau_{\rm iso}} \approx 1.285\frac{\tau_0}{\tau_{\rm iso}}, \tag{C4}$$

when $c = 2\ln 2$ and $N_c = 3$. We adopt this value for our

simulations where $N_c = 2$, since in previous studies of the stationary anisotropic situation little difference was found between the SU(2) and the SU(3) cases provided m_D was the same [31]. With our choice of an initial anisotropy given by $\tau_0/\tau_{\rm iso} = 10$, equating $\tau_0 = Q_s^{-1}$ and using units where $\tau_0 = 1$, the above result corresponds to the value $m_D = 3.585$ employed in Figs. 6–9.

The lower value $c \simeq 0.5$ for the gluon liberation factor corresponds to a smaller Debye mass, which turns out to be rather expensive in computer time, because one has then to go to much larger values of τ to obtain comparable effects and one cannot increase the time steps much without losing accuracy. However, in order to see the effect of this lower value of c (which now seems disfavored [56]), it should suffice to simply rescale the τ values of Figs. 6–9 such that the weak-field Abelian regime matches the semianalytical results presented in Fig. 1 of Ref. [34], where $c = 0.5$ was employed.

[1] M. J. Tannenbaum, Rep. Prog. Phys. **69**, 2005 (2006).
[2] D. Teaney, Phys. Rev. C **68**, 034913 (2003).
[3] P. Romatschke and U. Romatschke, Phys. Rev. Lett. **99**, 172301 (2007).
[4] H. Song and U. W. Heinz, Phys. Rev. C **77**, 064901 (2008).
[5] P. Kovtun, D. T. Son, and A. O. Starinets, Phys. Rev. Lett. **94**, 111601 (2005).
[6] S. M. H. Wong, Phys. Rev. C **54**, 2588 (1996).
[7] S. M. H. Wong, Phys. Rev. C **56**, 1075 (1997).
[8] R. Baier, A. H. Mueller, D. Schiff, and D. T. Son, Phys. Lett. B **502**, 51 (2001).
[9] P. Arnold, J. Lenaghan, and G. D. Moore, J. High Energy Phys. 08 (2003) 002.
[10] S. Mrówczyński, Phys. Lett. B **214**, 587 (1988).
[11] Y. E. Pokrovsky and A. V. Selikhov, JETP Lett. **47**, 12 (1988).
[12] S. Mrówczyński, Phys. Lett. B **314**, 118 (1993).
[13] A. H. Mueller, A. I. Shoshi, and S. M. H. Wong, Phys. Lett. B **632**, 257 (2006).
[14] D. Bödeker, J. High Energy Phys. 10 (2005) 092.
[15] P. Arnold and G. D. Moore, Phys. Rev. D **73**, 025013 (2006).
[16] A. H. Mueller, A. I. Shoshi, and S. M. H. Wong, Nucl. Phys. **B760**, 145 (2007).
[17] P. Arnold and G. D. Moore, Phys. Rev. D **76**, 045009 (2007).
[18] M. Asakawa, S. A. Bass, and B. Müller, Phys. Rev. Lett. **96**, 252301 (2006).
[19] E. S. Weibel, Phys. Rev. Lett. **2**, 83 (1959).
[20] P. Romatschke and M. Strickland, Phys. Rev. D **68**, 036004 (2003).
[21] P. Romatschke and M. Strickland, Phys. Rev. D **70**, 116006 (2004).
[22] B. Schenke, M. Strickland, C. Greiner, and M. H. Thoma, Phys. Rev. D **73**, 125004 (2006).
[23] B. Schenke and M. Strickland, Phys. Rev. D **74**, 065004 (2006).
[24] A. Rebhan, P. Romatschke, and M. Strickland, Phys. Rev. Lett. **94**, 102303 (2005).
[25] J.-P. Blaizot and E. Iancu, Phys. Rep. **359**, 355 (2002).
[26] R. D. Pisarski, arXiv:hep-ph/9710370.
[27] S. Mrówczyński and M. H. Thoma, Phys. Rev. D **62**, 036011 (2000).
[28] S. Mrówczyński, A. Rebhan, and M. Strickland, Phys. Rev. D **70**, 025004 (2004).
[29] P. Arnold and J. Lenaghan, Phys. Rev. D **70**, 114007 (2004).
[30] P. Arnold, G. D. Moore, and L. G. Yaffe, Phys. Rev. D **72**, 054003 (2005).
[31] A. Rebhan, P. Romatschke, and M. Strickland, J. High Energy Phys. 09 (2005) 041.
[32] P. Arnold and G. D. Moore, Phys. Rev. D **73**, 025006 (2006).
[33] D. Bödeker and K. Rummukainen, J. High Energy Phys. 07 (2007) 022.
[34] P. Romatschke and A. Rebhan, Phys. Rev. Lett. **97**, 252301 (2006).
[35] P. Romatschke and R. Venugopalan, Phys. Rev. Lett. **96**, 062302 (2006).
[36] P. Romatschke and R. Venugopalan, Phys. Rev. D **74**, 045011 (2006).
[37] E. Iancu and R. Venugopalan, in *Quark-gluon Plasma 3*, edited by R. C. Hwa and X.-N. Wang (World Scientific, Singapore, 2003), pp. 249–336.
[38] P. Arnold and P.-S. Leang, Phys. Rev. D **76**, 065012 (2007).
[39] A. Dumitru and Y. Nara, Phys. Lett. B **621**, 89 (2005).
[40] A. Dumitru, Y. Nara, and M. Strickland, Phys. Rev. D **75**, 025016 (2007).
[41] A. Dumitru, Y. Nara, B. Schenke, and M. Strickland, arXiv:0710.1223.
[42] J. Berges, S. Scheffler, and D. Sexty, Phys. Rev. D **77**, 034504 (2008).
[43] J. C. Taylor and S. M. H. Wong, Nucl. Phys. **B346**, 115 (1990).
[44] E. Braaten and R. D. Pisarski, Phys. Rev. D **45**, R1827 (1992).
[45] J. Frenkel and J. C. Taylor, Nucl. Phys. **B374**, 156 (1992).
[46] V. P. Nair, Phys. Rev. D **50**, 4201 (1994).
[47] J. P. Blaizot and E. Iancu, Nucl. Phys. **B417**, 608 (1994).
[48] J.-P. Blaizot and E. Iancu, Nucl. Phys. **B421**, 565 (1994).
[49] P. F. Kelly, Q. Liu, C. Lucchesi, and C. Manuel, Phys. Rev. D **50**, 4209 (1994).
[50] J. D. Bjorken, Phys. Rev. D **27**, 140 (1983).
[51] G. Baym, Phys. Lett. **138B**, 18 (1984).
[52] A. H. Mueller, Phys. Lett. B **475**, 220 (2000).
[53] T. Lappi and L. McLerran, Nucl. Phys. **A772**, 200 (2006).
[54] K. Fukushima, F. Gelis, and L. McLerran, Nucl. Phys. **A786**, 107 (2007).
[55] Y. V. Kovchegov, Nucl. Phys. **A692**, 557 (2001).

[56] T. Lappi, Eur. Phys. J. C **55**, 285 (2008).
[57] K. J. Eskola *et al.*, Phys. Rev. C **72**, 044904 (2005).
[58] J. P. Blaizot, E. Iancu, U. Kraemmer, and A. Rebhan, J. High Energy Phys. 06 (2007) 035.
[59] L. D. McLerran and R. Venugopalan, Phys. Rev. D **49**, 2233 (1994).
[60] R. Baier, A. H. Mueller, D. Schiff, and D. T. Son, Phys. Lett. B **539**, 46 (2002).
[61] A. Krasnitz and R. Venugopalan, Nucl. Phys. **A698**, 209 (2002).
[62] A. Krasnitz, Y. Nara, and R. Venugopalan, Nucl. Phys. **A727**, 427 (2003).